Temporal evolution of proto-Izu–Bonin–Mariana arc volcanism over 10 Ma: Constraints from statistical analysis of melt inclusion compositions

Morihisa Hamada[1*], Hikaru Iwamori[1,2,3], Philipp A. Brandl[4,5], Takayuki Ushikubo[6], Kenji Shimizu[6], Motoo Ito[6], He Li[7,8] & Ivan P. Savov[9]

[1]Solid Earth Geochemistry Research Group, Volcanoes and Earth's Interior Research Center, Research Institute for Marine Geodynamics, Japan Agency for Marine-Earth Science and Technology, 2-15 Natsushima-cho, Yokosuka 237-0061, Japan

[2]Department of Earth and Planetary Sciences, Tokyo Institute of Technology, 2-12-1 Meguro-ku, Tokyo 152-8551, Japan

[3]Earthquake Research Institute, University of Tokyo, 1-1-1 Yayoi, Bunkyo-ku, Tokyo 113-0032, Japan

[4]GEOMAR Helmholtz Centre for Ocean Research Kiel, Wischhofstr. 1-3, 24148 Kiel, Germany

[5]Research School of Earth Sciences, The Australian National University, 142 Mills Road, Acton ACT2601, Australia

[6]Kochi Institute for Core Sample Research, Japan Agency for Marine-Earth Science and Technology, 200 Monobe-otsu, Nankoku, Kochi 783-8502, Japan

[7]Center of Deep Sea Research, Institute of Oceanology, Chinese Academy of Sciences, 7 Nanhai Road, Qingdao 266071, China

[8]Laboratory for Marine Mineral Resources, Qingdao National Laboratory for Marine Science and Technology, Qingdao 266237, China

[9]Institute of Geophysics and Tectonics, School of Earth and Environment, University of Leeds, Leeds LS2 9JT, United Kingdom

*Corresponding author: mhamada@jamstec.go.jp, Tel. +81-46-867-9808

Abstract

International Ocean Discovery Program (IODP) Expedition 351 "Izu–Bonin–Mariana (IBM) Arc Origins" drilled Site U1438, situated in the north-western region of the Philippine Sea. Here volcaniclastic sediments and the igneous basement of the proto-IBM volcanic arc were recovered. To gain a better understanding of the magmatic processes and evolution of the proto-IBM arc, we studied melt inclusions hosted in fresh igneous minerals and sampled from 30- to 40-Ma-old deposits, reflecting the maturation of arc volcanism following subduction initiation at 52 Ma. We performed a novel statistical analysis on the major element composition of 237 representative melt inclusions selected from a previously published dataset, covering the full age range between 30 and 40 Ma. In addition, we analysed volatiles (H_2O, S, F and Cl) and P_2O_5 by Secondary Ion Mass Spectrometry (SIMS) for a subset of 47 melt inclusions selected from the dataset. Based on statistical analysis of the major element composition of melt inclusions and by considering their trace and volatile element compositions, we distinguished five main clusters of melt inclusions, which can be further separated into a total of eight subclusters. Among the eight subclusters, we identified three major magma types: (1) enriched medium-K magmas, which form a tholeiitic trend (30–38 Ma); (2) enriched medium-K magmas, which form a calc-alkaline trend (30–39 Ma); and (3)

depleted low-K magmas, which form a calc-alkaline trend (35–40 Ma). We demonstrate that (1) the eruption of depleted low-K calc-alkaline magmas occurred prior to 40 Ma and ceased sharply at 35 Ma; (2) the eruption of depleted low-K calc-alkaline magmas, enriched medium-K calc-alkaline magmas and enriched medium-K tholeiitic magmas overlapped between 35 and 38−39 Ma; and (3) the eruption of enriched medium-K tholeiitic and enriched medium-K calc-alkaline magmas became predominant thereafter at the proto-IBM arc. Identification of three major magma types are distinct from the previous work, in which enriched medium-K calc-alkaline magmas and depleted low-K calc-alkaline magmas were not identified. This indicates the usefulness of our statistical analysis as a powerful tool to partition a mixture of multivariable geochemical datasets, such as the composition of melt inclusions in this case. Our data suggest that a depleted mantle source had been replaced by an enriched mantle source due to convection beneath the proto-IBM arc from >40 to 35 Ma. Finally, thermodynamic modelling indicates that the overall geochemical variation of melt inclusions assigned to each cluster can be broadly reproduced either by crystallisation differentiation assuming P = 50 MPa (~2-km deep) and ~2 wt % H_2O (almost saturated H_2O content at 50 MPa) or P = 300 MPa (~15-km deep) and ~6 wt % H_2O (almost saturated H_2O content at 300 MPa). Assuming oxygen fugacity (f_{O2}) of log f_{O2} equal to +1 relative to nickel-nickel oxide (NNO) buffer best

reproduces the overall geochemical variation of melt inclusions, but assuming a more oxidising conditions (log f_{O2} = +1 to +2 NNO) likely reproduces the geochemical variation of enriched medium-K and calc-alkaline melt inclusions (30−39 Ma).

Key words: Izu–Bonin–Mariana arc, Volatiles, Melt inclusion, Amami Sankaku Basin, International Ocean Discovery Program, Statistical analysis

INTRODUCTION

The Izu–Bonin–Mariana (IBM) arc-basin system in the Western Pacific (Fig. 1) is an ideal setting for studying subduction initiation and the evolution of arc volcanism because the age and duration of geological events, temporal changes in magmatic composition, and the precise seismic structure have been extensively studied (e.g. Stern & Bloomer, 1992; Taylor, 1992; Arculus *et al.*, 1995; Stern, 2002, 2004; Stern *et al*., 2003; Taylor & Goodliffe, 2004; Hickey-Vargas *et al.*, 2006; Ishizuka *et al.*, 2006, 2011a, 2011b; Reagan *et al.*, 2008, 2010, 2017, 2019; Straub *et al*., 2010, 2015). Such studies include several deep sea drilling expeditions that targeted the IBM arc-basin system, including forearc Sites 778−780 (Fryer *et al.*, 1995, and references therein), Sites 782 and 786 (Pearce *et al*., 1992a, 1992b; Straub & Layne, 2003a, 2003b), Sites U1439−U1442 (Reagan *et al*., 2017; Shervais *et al.*, 2019), Sites U1491−U1498 (Fryer *et al.*, 2017), rear-arc Sites U1436 and U1437 (Busby *et al*., 2017), and rear-arc Site 1201 (Savov *et al.*, 2006). International Ocean Discovery Program (IODP) Expedition 351 'Izu–Bonin–Mariana Arc Origins' (June−July 2014) aimed at improving our understanding of how subduction initiated and how island arcs evolved thereafter. This expedition drilled Site U1438 (27˚23'N, 134˚19'E, water depth 4700 m) in the Amami Sankaku Basin (ASB), situated in the north-western region of the Philippine Sea (Fig. 1).

The magmatic evolution of the IBM arc-basin system can be reconstructed from the geochemistry of melt inclusions hosted in fresh igneous minerals that are recovered throughout the sequence of coarse (sand to gravel) volcaniclastic sediments, because melt inclusions can be protected from surface processes after entrapment in their host minerals, if these are chemically and physically stable. Brandl *et al*. (2017) have analysed the major, trace and volatile elements (S and Cl) of 304 melt inclusions hosted in fresh clinopyroxene and plagioclase grains from well-dated volcaniclastic sediments of Unit III of the core ranging from 30 Ma (Rupelian; Lower Oligocene) to 40 Ma (Bartonian; Middle Eocene) (Fig. 2), and discussed the temporal evolution of the proto-IBM arc volcanism. They concluded that (1) volcanism of the proto-IBM arc shifted gradually from calc-alkaline to tholeiitic affinity with time (30−40 Ma); and (2) such a compositional shift is linked to both the volcanic productivity and the maturation of an evolving island arc. We will use the terms 'tholeiitic' and 'calc-alkaline' to refer to rock series or differentiation trends, including andesite and more silicic rocks, using the SiO_2 versus total FeO/MgO diagram of Miyashiro (1974).

In this study, we applied a statistical analysis of the published dataset of melt inclusion compositions by Brandl *et al*. (2017). Statistical analysis aids in partitioning a mixture of multivariable geochemical datasets and potentially helps us to reconstruct their

geological evolution (e.g. Iwamori *et al*., 2017). The purpose of this study is to differentiate a multivariable geochemical dataset of melt inclusions into several petrogenetically distinct groups and constrain their origins. The geochemical dataset of melt inclusions by Brandl *et al*. (2017) can represent a "mixture" of volcaniclastic sediments sourced from volcanic centres of the Kyushu–Palau Ridge (KPR), which is about 100 km east and upslope of Site U1438 (Fig. 1). The KPR is the remnant part of the currently active IBM arc and was active between 25 and 49 Ma (Ishizuka *et al.*, 2011b, 2018). In addition, we analysed a subset of 47 carefully selected melt inclusions for their volatiles (H_2O, S, F and Cl) and P_2O_5 content using Secondary Ion Mass Spectrometry (SIMS) to extend the dataset of Brandl *et al*. (2017) and better constrain the temporal evolution of the proto-IBM arc volcanism from 30 to 40 Ma.

LITHOSTRATIGRAPHY OF SITE U1438

The IBM arc is an intra-oceanic convergent margin system that extends approximately 2500 km south of Honshu, Japan (Fig. 1). Volcanism of the proto-IBM arc began in the middle Eocene (52 Ma; Ishizuka *et al.*, 2018) with the onset of subduction of the Mesozoic (120−130 Ma; Nakanishi *et al.*, 1992) Pacific Plate beneath the Philippine Sea Plate. The volcanism of proto-arc basalts (48−52 Ma; Reagan *et al.*, 2008,

2010; Ishizuka *et al.*, 2011a, 2014a, 2018), which formed the at least 250 km wide pre-arc igneous basement under an extensional stress field (Arculus *et al.*, 2015a; Reagan *et al.*, 2017), was followed by boninitic volcanism during the middle Eocene (44−48 Ma, Ishizuka *et al.*, 2006, 2011a, 2018; Kanayama *et al*., 2012, 2014; Umino *et al*., 2015; Reagan *et al*., 2010, 2019). Boninitic volcanism ceased at 44 Ma and was followed by coeval eruptions of arc tholeiitic and calc-alkaline magmas (Ishizuka *et al.*, 2006; Kanayama *et al.*, 2014). The proto-Izu-Bonin arc experienced a quiescence of volcanism at 20−23 Ma, which coincides with the period of arc rifting and opening of the Shikoku and Parece Vela backarc basins (e.g. Stern, 2004).

Gravity flows repeatedly transported material from arc volcanic complexes of the KPR to Site U1438 in the ASB, which were likely triggered by large-volume volcanic eruptions and/or flank collapses (Johnson *et al.*, 2017). While proto-arc basalts (48−52 Ma), boninites (44−48 Ma) and subsequent volcanic rocks representing the initial stages of arc volcanism are exposed in the forearc region of the currently active IBM arc (e.g. Ishizuka *et al.*, 2006, 2011a, 2018; Reagan *et al.*, 2010, 2019; Straub *et al*., 2010; Kanayama *et al*., 2012), few corresponding geological units have been recovered at the rear-arc side to date. Ishizuka *et al.* (2011b) systematically sampled submarine volcanic rocks along the KPR via dredging; however, their $^{40}Ar/^{39}Ar$ ages covered only the

youngest stages of the KPR volcanism (25−28 Ma; Ishizuka *et al.*, 2011b; Straub *et al.*, 2010), when magmatic activity of the proto-IBM arc ceased through arc rifting and backarc spreading (e.g. Stern, 2004). Studies using drill cores from Site 1201, located at the rear-arc side of the KPR and about 900 km south of Site U1438, found clues to the magmatic history of the proto-IBM arc from the Eocene to the Oligocene (30−35 Ma; Savov *et al.*, 2006). Thus, the drill cores from Site U1438 were expected to complement our knowledge of the magmatic history of the proto-IBM rear-arc between the formation of proto-arc basalts (48−52 Ma) and the cessation of arc volcanism along the KPR (25−28 Ma) (Ishizuka *et al.*, 2011b; Straub *et al.*, 2010).

The recovered 1611 m long core at Site U1438 is composed of a 1461 m thick sedimentary section and 150 m of igneous basement rocks. The good recovery (76%) of the sedimentary section allowed us to reconstruct the magmatic history of the proto-IBM arc in detail (Brandl *et al.*, 2017; Johnson *et al.*, 2017). The sedimentary section is subdivided into four units based on lithology (Fig. 2; Arculus *et al.*, 2015a, 2015b). The uppermost sedimentary Unit I (160.3 m thick) is Holocene to late Oligocene in age and thus, postdates rifting of the proto-IBM arc. It is composed of hemipelagic fine-grained sediments interbedded with discrete ash layers likely derived from explosive eruptions along the nearby Ryukyu and Kyushu arcs (e.g. Kimura *et al.*, 2015). Unit II (139.4 m

thick) is Oligocene in age and is composed of turbidites (silt−very fine sand). Unit III (1046.4 m thick) is Oligocene to Eocene in age and is composed of coarser-grained turbidites (medium to very coarse sand to gravel) relative to Unit II. Unit IV (99.7 m thick) is composed of siliceous pelagic sediments interbedded with tuffaceous sand and volumetrically minor intrusive rocks that possibly reflect the slow onset of arc volcanism. The age of Unit IV is 42−49 Ma (Fig. 2), overlapping the age of boninitic volcanism at the IBM arc (44−48 Ma). The deposition age of volcaniclastic sediments is based on the age-depth model of Brandl *et al*. (2017), which is consistent with the U−Pb geochronology (Barth *et al.*, 2017) and the shipboard chronostratigraphy (Arculus *et al*., 2015a, 2015b). Most of the sedimentary units thicken eastwards (Arculus *et al*., 2015b), indicating that volcaniclastic sediments are sourced from the KPR at the eastern boundary of the ASB (Fig. 1). The drilled interval of the igneous basement rock Unit 1 is 150 m thick with 29% recovery. The geochemistry of the igneous basement rocks of the ASB (Arculus *et al.*, 2015a; Hickey-Vargas *et al.*, 2018; Yogodzinski *et al.*, 2018) and their age (46.8−49.3 Ma; Ishizuka *et al.*, 2018) are similar to those of proto-arc basalts of the forearc region of the IBM arc dated at 50−52 Ma (Reagan *et al.*, 2008, 2010; Ishizuka *et al.*, 2011a, 2014a).

ANALYSIS OF VOLATILES IN MELT INCLUSIONS

Samples

The 2−4 cm long half core sections of volcaniclastic sediments were electrically fragmented using the 'Selfrag Lab' at the Japan Agency for Marine-Earth Science and Technology (JAMSTEC). Fresh silicate minerals containing glassy melt inclusions were handpicked from the fragmented samples under a binocular microscope, mounted on epoxy resin and polished until the melt inclusions were exposed on the surface. Clinopyroxene and plagioclase were the predominant minerals hosting melt inclusions. Orthopyroxene, quartz and amphibole also hosted limited melt inclusions. The shipboard XRD analysis (Arculus *et al*., 2015b) indicated the presence of quartz being restricted to the deeper levels of Unit III (>1120 mbsf). Olivine was not recovered from any samples of Unit III (Brandl *et al.*, 2017).

Representative back-scattered electron (BSE) images of melt inclusions are shown in Fig. 3(a−c). Plagioclase-hosted melt inclusions (<50 μm in diameter) are usually rounded (Fig. 3a). Most of the clinopyroxene-hosted melt inclusions (<100 μm in diameter) are either rounded (Fig. 3b) or slightly angular (Fig. 3c). Shrinkage bubbles are observed in some clinopyroxene-hosted melt inclusions (Fig. 3c). Typically, post-entrapment overgrowth of the host minerals inside the melt inclusions were not

identifiable. All analysed melt inclusions are glassy, suggesting that they were rapidly quenched after eruption. We did not analyse altered melt inclusions or melt inclusions with observed daughter minerals. In addition to glass as melt inclusions, tiny minerals (<100 μm long) are sometimes trapped as inclusions. For example, Fig. 3d is a BSE image of apatite and Fe-Ti oxide inclusions hosted by clinopyroxene.

We checked the apparent Fe-Mg partitioning between clinopyroxene host and coexisting melt inclusions to ensure that the composition of clinopyroxene-hosted melt inclusions represents the original melt compositions before entrapment. In this study, we excluded 67 clinopyroxene-hosted melt inclusions for which $K_D(Fe\text{-}Mg)^{cpx\text{-}melt} \leq 0.2$ from the dataset of 304 melt inclusions reported by Brandl *et al*. (2017). We assumed that melt inclusions for which $K_D(Fe\text{-}Mg)^{cpx\text{-}melt} \leq 0.2$ are in disequilibrium with host clinopyroxene ($K_D(Fe\text{-}Mg)^{cpx\text{-}melt}$ is 0.28 ± 0.08; Putirka, 2008) and do not represent original melt compositions, due to post-entrapment overgrowth of host clinopyroxene and significant compositional modification of melt inclusions. This results in a total of 237 melt inclusions used for this study (Supplementary Data Table S1).

Analytical methods

We carefully selected a subset of 47 representative melt inclusions (42

clinopyroxene-hosted and 5 plagioclase-hosted melt inclusions) from the dataset of Brandl *et al*. (2017), and then analysed them for their volatiles (H_2O, S, F and Cl) and P_2O_5 content using SIMS. We used the Cameca IMS-1280HR at the Kochi Institute for Core Sample Research of JAMSTEC. Our samples (wafer containing one-side intersected melt inclusions) were originally mounted in epoxy, polished, and then carbon-coated for major element analyses using Electron Probe MicroAnalysers (EPMA; Brandl *et al*., 2017). Prior to the analysis with SIMS, we removed the carbon coatings and mounted the samples in indium metal. The samples were cleaned using acetone and distilled water in an ultrasonic bath, and then were dried in a high-vacuum oven (10^{-7} torr) at 90 ˚C for several days (>48 h). After drying, the samples were coated with Au to avoid charge build-up during the SIMS analyses. Samples were then stored in the airlock chamber of the SIMS at $<10^{-8}$ torr for >48 h to improve vacuum conditions before starting the analytical session (Shimizu *et al*., 2017). The analyses were carried out with a ~15 μm defocused Cs^+ ion beam and an ion potential of 20 kV (10 kV at the ion source and 10 kV at the sample surface). A normal-incidence electron gun was used for charge compensation of the sample surface. Secondary ions ($^{16}OH^-$, $^{19}F^-$, $^{30}Si^-$, $^{31}P^-$, $^{32}S^-$, and $^{35}Cl^-$) were accelerated by −10 kV and were detected by an axial electron multiplier using a magnetic peak-switching method. The mass-resolving power was set to ~6000. Further

details of the analytical conditions and results of a suite of basaltic reference glasses is presented in Shimizu *et al.* (2017). The volatile element content of the basaltic reference glasses (vol-0B, vol-005B, vol-05A, vol-1B, vol-3A, EPR-G3, IND-G1, FJ-G2, MRN-G1, MA42, BCR-2G, BIR-1G and BHVO-1G) ranges from 0−4.8 wt % for H_2O, 8−1018 ppm for F, 12−2833 ppm for Cl, 0−1372 ppm for S, and 0.027 −0.370 wt % for P_2O_5. An internal reference glass EPR-G3 was mounted together with the samples in each indium mount to monitor for potential instrumental drift and check the reproducibility of the analytical results. We excluded CO_2 analyses due to the potential contamination of carbon resulting from the prior carbon coating for analyses with EPMA (e.g. Shimizu *et al.*, 2009).

The matrix effects of SIMS on volatile element content should be considered because we used basaltic reference glasses and analysed melt inclusions ranging widely from basaltic to rhyolitic compositions. The H_2O content of silicic melt inclusions analysed with SIMS is expected to be lower than the true H_2O content because of the matrix effects, while the S, F and Cl content is not affected (e.g., Hauri *et al*., 2002; Druitt *et al*., 2016). Thus, we additionally analysed the H_2O content of six silicic (dacitic and rhyolitic) melt inclusions using a Fourier Transform InfraRed (FTIR) spectrometer at JAMSTEC. Details of additional analyses and results are described in Supplementary

Appendix.

Results of the volatile element analyses of melt inclusions

The results of the volatile element analyses combined with the results of the major and trace element analyses of Brandl *et al.* (2017) are summarised in Supplementary Data Table S1. The average values of 2σ deviation of the SIMS analyses are 100 ppm for H_2O, 2 ppm for F, 4 ppm for Cl, 14 ppm for S and 30 ppm for P_2O_5 based on repeated analyses of EPR-G3 reference glass (Shimizu *et al.*, 2017 & 2019). Among the elements analysed with SIMS in this study, P_2O_5, Cl and S have already been analysed with EPMA and published by Brandl *et al*. (2017). We used analytical data of these elements acquired either by SIMS or EPMA in this study. We used P_2O_5 content analysed with SIMS, because the analytical uncertainty of P_2O_5 with SIMS (2σ = 30 ppm) is much smaller than that with EPMA (2σ = 0.1 wt %). We used Cl content (< 6000 ppm) analysed with SIMS, because the analytical uncertainty of Cl with SIMS (2σ = 4 ppm) is much smaller than that with EPMA (2σ = 200 ppm). However, we consider the analytical results with EPMA to be more reliable for high-Cl melt inclusions (>8000 ppm), because the reference glasses for SIMS analysis have a range of Cl content from 12 to 2833 ppm, thus extrapolating the calibration line of Cl toward >8000 ppm may not be reasonable. We

used the S content determined with SIMS if analytical data with both methods were available, because (i) the analytical uncertainty of S with SIMS (2σ = 14 ppm) is much smaller than that with EPMA (2σ = 200 ppm) and (ii) the wavelength of the SKα X-ray changes as a function of the oxidation state of S, which can result in underestimation of the S content when using EPMA. Further details on comparison of P_2O_5, Cl and S content analysed by both methods are described in Supplementary Appendix and Fig. S1. Regarding the H_2O content of six silicic melt inclusions, analytical results with FTIR were higher than those with SIMS because of the matrix effect. The differences in analytical results between the two methods are systematically larger with increasing SiO_2 (Supplementary Appendix, Fig. S2). In this study, we used the H_2O data analysed with FTIR for these six silicic melt inclusions. Further details are described in Supplementary Appendix.

Analytical data of volatile elements of melt inclusions are summarised in Fig. 4, where they are plotted against the deposition age. The analyses cover a wide range of volatile element content. For example, H_2O ranges from 1.4 wt % to 6.9 wt % (Fig. 4a) and S ranges from ~10 ppm to 3000 ppm (Fig. 4b). Generally, the upper limit of volatile element content, excluding three high-Cl melt inclusions (>8000 ppm; Fig. 4d), increases with decreasing age, along with that of incompatible element oxides such as P_2O_5 (Fig.

4e). The H_2O content decreases from basalt to andesite, but increases again with increasing SiO_2 toward rhyolitic composition (Fig. 5a). Sulphur content monotonously decreases with increasing SiO_2 (Fig. 4b) and show a broad correlation with FeO_t, which is total iron oxides ($FeO + Fe_2O_3$, Fig. 5c). Fluorine content correlates with K_2O ($\leq$ 1.5 wt %; Fig. 5d). Chlorine also correlates with K_2O, except for high-Cl melt inclusions (>8000 ppm; Fig. 5e). Fluorine and phosphorous have a similar incompatibility during melting and crystallisation; therefore, the F/P ratio of melt inclusions can reflect that of the mantle source (Saal *et al*., 2002). The F/P ratio in elemental weight is relatively constant (0.3−0.8) at $SiO_2 \leq 60$ wt % and increases to as much as 4.4 at $SiO_2 \geq 70$ wt % at younger ages (Figs. 4f and 5f).

STATISTICAL ANALYSIS OF MELT INCLUSION COMPOSITIONS

Methods

Volcaniclastic sediments can be sourced from multiple volcanic centres in the upslope vicinity of Site U1438. Thus, melt inclusion compositions may represent a mixture of volcaniclastic sediments sourced from multiple vent sites, possibly not only from the KPR but, depending on the plate configuration, also from the frontal arc section of the proto-IBM arc. In addition, they could include volcaniclastic material from primary

eruptions and reworked sediments.

The statistical analysis of multivariable datasets of such a mixture of materials is thus a useful approach and may help to reconstruct their geological evolution. Statistical approaches commonly used in petrology and geochemistry include principal component analysis (PCA) (e.g. Zindler *et al*., 1982; Allègre *et al*., 1987; Hart *et al*., 1992; Stracke, 2012; Ueki & Iwamori, 2017), factor analysis (White & Duncan, 1996), independent component analysis (Iwamori & Albarède, 2008; Iwamori & Nakamura, 2012, 2015; Yasukawa *et al*., 2016), K-means cluster analysis (KCA) (e.g. Temple *et al.*, 2008; Brandmeier & Wörner, 2016), and implementation of machine learning techniques (e.g. Kuwatani *et al*., 2014; Petrelli & Perugini, 2016; Ueki *et al*., 2018). Iwamori *et al*. (2017) demonstrated that the structure of a multivariable dataset is best resolved when: (1) PCA is applied to the dataset; and (2) the eigenvalue normalised-PC scores (which are called 'whitened data') are partitioned by KCA. PCA is commonly used for effectively specifying the uncorrelated base vectors that account for the variance. KCA is also a common statistical method used to partition the multivariate dataset into an assigned number of clusters *K*, in which the total distance between the mean of a cluster and the individual data points in the cluster is minimised (e.g. MacQueen, 1967, and references therein).

In this study, we applied PCA and KCA to the major element compositions (10 elements) of 237 melt inclusions, following the procedures of Iwamori *et al*. (2017). We did not include S and Cl content into our dataset to perform statistical analysis because: (1) some melt inclusions are devoid of S and Cl content (Table S2 of Brandl *el al.*, 2017); and (2) volatile elements are subject to degassing. First, the raw geochemical data of the 237 melt inclusions, which are imposed by a constant-sum (normalised to 100 wt %) constraint, were transformed into logarithmic space by performing centred log-ratio transformation (e.g. Aitchison, 1982, 1984, 1986). Then, the data were processed by primary standardisation using the mean and standard deviation. Next, 'whitening' (division of PC scores by the square root of the eigenvalues) was applied to the dataset to decorrelate the variables. Based on the eigenvalues and eigenvectors, a minimum number of variables that account for a sufficiently large proportion (i.e. $\geq$ 90%) of the sample variance were chosen. The number of eigenvectors that individually account for $\geq$ 5% of the variance for the dataset of 237 melt inclusions is 5 (Fig. 6a). In addition, the cumulative contribution of the first five eigenvectors accounts for ~90 % of the variance (Fig. 6b), which suggests that the number of variables can be reduced from 10 (number of elements) to five or slightly more eigenvectors (Iwamori *et al*., 2017). Then, we performed KCA on the pre-processed data from 100 random and different initial

conditions by varying *K* from 4 to 12 and varying the number of independent components (nic) from 3 to 8. We finally found that the geochemical dataset of melt inclusions consists of essentially five clusters with five independent components (*K* = 5 and nic = 5). Results of statistical analysis of the 237 melt inclusions by KCA, including their principal components and independent components are given in Supplementary Data Table S2.

Results of statistical analyses

The results of KCA are summarised in oxide variation diagrams (Fig. 7). Further details of the results are summarised in Figs. S3 and S4 of Supplementary Appendix. Downhole distributions of melt inclusions assigned to each cluster are summarised in Fig. 8. Cluster 1 melt inclusions (*n* = 84) are medium-K mafic melts which form a tholeiitic differentiation trend (Figs. 7e and g) and occur from 38 to 30 Ma (Fig. 8a). They are characterised by higher TiO_2, suggesting that they represent melts from a fertile mantle source. Cluster 2 melt inclusions (*n* = 61) form a calc-alkaline differentiation trend (Fig. 7d) and can be separated further into two individual subclusters in terms of K_2O (Fig. 7g): Cluster 2a melt inclusions (*n* = 2) are high-K melts and Cluster 2b melt inclusions (*n* = 59) are medium-K melts. Cluster 2a melt inclusions only occur at ~30 Ma, while Cluster 2b melt inclusions occur at the full range from 30 to 40 Ma (Fig. 8). Cluster 3 melt

inclusions (n = 67) are low-K melts which form a calc-alkaline differentiation trend (Figs. 7d and g). They can be further separated into two individual subclusters: Cluster 3a melt inclusions (n = 2) are characterised by higher Al_2O_3 (Fig. 7b) and lower MgO (Fig. 7e) at given SiO_2 than Cluster 3b melt inclusions (n = 65). Clusters 3a and 3b can also be distinguished in terms of their ages; the former occur at ~30 Ma, while the latter occur from 35 to 40 Ma (Fig. 8). Cluster 4 melt inclusions (n = 22) are dacitic and rhyolitic melts which form a calc-alkaline trend. They can be separated further into two individual subclusters: the Cluster 4a melt inclusion (n = 1) is distinguished in terms of lower Al_2O_3 (Fig. 7b), higher FeO_t (Fig. 7c) and lower K_2O (Fig. 7g) than Cluster 4b melt inclusions (n = 21) at given SiO_2. Clusters 4a and 4b can also be distinguished in terms of their ages; the former occur at ~37 Ma, while the latter occur at ~30 Ma (Fig. 8). Cluster 5 melt inclusions (n = 3) are characterised by low P_2O_5 (~ 0 wt %; Fig. S4j of Supplementary Appendix and Supplementary Data Table S1).

Twenty-five whole-rock core samples contain melt inclusions assigned to more than one cluster (Fig. 8a), suggesting that the whole-rock core samples are in fact mixtures of volcaniclastic sediments from different volcanic series. Such volcaniclastic sediments might have been mixed during long-distance transport by gravity flow and deposited around Site U1438. The 237 melt inclusions included in this study are hosted in 145

individual host minerals. In the case where two or more melt inclusions are hosted in one single host mineral, these melt inclusions usually fall into an identical cluster. However, we found 11 exceptional clinopyroxene minerals hosting two or more melt inclusions that are assigned to different clusters (Fig. 8b and Table 1). Most of these cases can be explained by heterogeneity of the host minerals. For example, three host clinopyroxene minerals (D19R3B-min1, D55R3A-min2 and D31R6-min5) are zoned, and the melt inclusions located at the different zones are assigned to different clusters (Figs. 9a–c). However, the case of the clinopyroxene D55R3B-min3 (Fig. 9d) is more complicated: a low-Fe zone is surrounded by a middle- to high-Fe zone and the melt inclusions are located around the low-Fe zone. Melt inclusions #2, #3 and #4 (Cluster 1) are hosted by high-Fe clinopyroxene and melt inclusions #5 and #6 (Cluster 2b) are hosted by middle-Fe clinopyroxene, although the compositional zoning from the middle- to high-Fe zone is gradual. Melt inclusions hosted by this clinopyroxene D55R3B-min3 are characterized by high-Cl content of up to ~10000 ppm (Figs. 4d and 5e). The origin of these high-Cl melt inclusions will be discussed later. In another case, two melt inclusions, which are assigned to different clusters, are hosted in a homogeneous clinopyroxene mineral (D27R3B-min4; Fig. 9e). This shows that heterogeneity of the host minerals is not the sole explanation for melt heterogeneity.

The temporal evolution of the melt as reflected by SiO_2, TiO_2, Al_2O_3, FeO_t, MgO, CaO and K_2O content is shown in Fig. 10 and interpreted in Fig. 11. It is important to note that the ages of the first appearance of Clusters 1 (38 Ma), 2b (39 Ma) and 3b (40 Ma) are significantly different, although the data are sparse for this time period (38−40 Ma).

Characteristics of volatile elements in each cluster

The results of the volatile element analyses of melt inclusions, combined with the results of KCA, are presented in Fig. 12. Analytical data of volatile elements are available for Clusters 1, 2b, 3b and 4b melt inclusions. We distinguished two coeval subgroups in Cluster 3b melt inclusions: a low-H_2O subgroup and a high-H_2O subgroup (Figs. 11 and 12). Both subgroups represent magmas that erupted simultaneously in the period from 40 to 35 Ma. Some Clusters 1 and 3b (high-H_2O subgroup) melt inclusions (such as D20R4B-min2-mi1 and D27R3B-min4-mi2) contain 6–7 wt % H_2O, which is the maximum range of H_2O content of melt inclusions reported from island arcs (e.g. Plank *et al.*, 2013; 2−6 wt %). Generally, the H_2O content of melt inclusions decreases from 50 to 60 wt % SiO_2 but increases again in from 60 to 70 wt % SiO_2 (Fig. 12a). In terms of sulphur content, systematic differences are observed among the four clusters.

Some Cluster 1 melt inclusions enriched in H_2O are also enriched in sulphur, and the maximum sulphur content of Clusters 1, 2b, 3b and 4 melt inclusions is ~3000 ppm (D27R3B-min4-mi2), ~760 ppm, ~1200 ppm and ~260 ppm, respectively (Figs. 12b and c). The sulphur content monotonously decreases with increasing SiO_2 (Fig. 12b).

The F content linearly correlates with K_2O (≤1.5 wt %), except for the Cluster 4b melt inclusions when $K_2O \geq 1.5$ wt % (Fig. 12d). The Cl content also positively correlates with K_2O, except for three high-Cl (up to ~10,000 ppm) melt inclusions (D55R3B-min3-mi2, D55R3B-min3-mi3 and D55R3B-min3-mi5), all of which are hosted in a single clinopyroxene D55R3b-min3 (Figs. 9d and 12e). The F and Cl content of Cluster 3b melt inclusions is lower than that in the other clusters (Figs. 12d and 12e). The deviation of the F/P ratio is relatively small (0.3−0.8) at $SiO_2 \leq 60$ wt % (Clusters 1, 2b and 3b), which reflects that of the mantle source (Saal *et al*., 2002). The differences in the F/P ratio (0.3−0.8) are due to the differences in P_2O_5 content of the melt inclusions; higher F/P ratios (~0.8) correspond to low-P_2O_5 (around 0.1 wt %) and lower F/P ratios (~0.3) correspond to high-P_2O_5 (0.2−0.3 wt %) (Fig. 12f). The F/P ratio significantly increases from 1 to 5 at $SiO_2 \geq 70$ wt % (Cluster 4b; Fig. 12f).

Characteristics of trace elements in each cluster

Brandl *et al*. (2017) analysed the trace element compositions of selected melt inclusions by Laser Ablation-Inductively Coupled Plasma-Mass Spectrometry (LA-ICP-MS; Supplementary Data Table S1). Trace element patterns of 34 selected melt inclusions, assigned to Clusters 1, 2b, 3b, 4a and 4b are normalised to the Depleted Mid-Ocean Ridge Basalt (MORB) Mantle (DMM; Workman & Hart, 2005) and presented in Figs. 13a−d. Trace element compositions of melt inclusions assigned to other clusters are not available in this study. Figures 13a−d also indicates the compositional ranges of selected trace element ratios (La/Yb, Nb/Zr and Zr/Yb ratios) of melt inclusions. Trace element patterns of arc tholeiitic and calc-alkaline series rocks (40−45 Ma; Kanayama *et al*., 2014) and boninites (44−48 Ma; Umino *et al.*, 2015) from the Ogasawara (Bonin) islands, an uplifted segment of the proto-IBM forearc, are also shown for comparison (Figs. 13e−g). It is important to note, however, that the latter suites from the frontal proto-IBM arc volcanoes (40−48 Ma; Kanayama *et al.*, 2014 and Umino *et al*., 2015) may not be directly comparable with our rear-arc melt inclusions (30−40 Ma).

The trace element patterns of Clusters 1 and 2b melt inclusions (Figs. 13a and b) overlap as a whole, with a few exceptions (U1438E-13R2W-I1 (Fig. 13a) and U1438D-15R1W-I3 (Fig. 13b)). Some Cluster 1 melt inclusions are characterised by depletion of the high field-strength elements (HFSEs) such as Zr and Hf (Fig. 13a). In contrast, Cluster

2b melt inclusions show no obvious depletions of HFSEs. An andesitic Cluster 2b melt inclusion (U1438D-15R1W-I3) shows a different trace element pattern than others in the same cluster, which are either basalt or basaltic andesite (Fig. 13b). The trace element patterns of Cluster 1 melt inclusions (30−38 Ma) and Cluster 2b melt inclusions (30−39 Ma) are similar but not comparable to those of the tholeiitic and calc-alkaline series rocks of the Ogasawara (Bonin) islands (40−45 Ma; Kanayama *et al*., 2014), respectively (Figs. 13d and e). The trace element patterns of Clusters 3b and 4a melt inclusions are almost identical (Fig. 13c). Combined with major element composition, Cluster 4a lies on the trend of Cluster 3b in the SiO_2-K_2O space (Fig. 7g). This observation indicates that melt inclusions assigned to Clusters 3b and 4a can be derived from the same mantle source. Cluster 3b melt inclusions (35−40 Ma; Fig. 13c) are not directly comparable to boninites (44−48 Ma; Fig. 13g). Silicic melt inclusions assigned to Cluster 4b show higher trace element abundances with TiO_2 depletion (Fig. 13d).

DISCUSSION

Origin of the high Cl melt inclusions

Three melt inclusions hosted in a single clinopyroxene D55R3B-min3 (host mineral ID 60; Table 1) contain high Cl content up to ~10000 ppm (Fig. 12e). Straub &

Layne (2003a, b) recognised 'halogen-rich andesites' at their IBM fore-arc sites, where they report enriched F (up to 900 ppm) and Cl (up to 9000 ppm) (Figs. 14a and b). The three Cl-rich melt inclusions hosted by clinopyroxene D55R3B-min3 contain only ~400 ppm F (Fig. 14c), while their Cl content surges to up to 10000 ppm (Fig. 14d), and therefore they cannot be melts associated with 'halogen-rich andesites' as proposed by Straub & Layne (2003a, b). We infer that brine assimilation likely explains the origin of the three Cl-rich melt inclusions. Brine assimilation has been commonly proposed at mid-ocean ridges and ocean islands to explain extraordinarily high Cl content of melt inclusions (e.g. Michael & Cornell, 1998; Coombs *et al*., 2004), but also occur at submarine arc volcanic systems (Ishizuka *et al*., 2014b). Among the three melt inclusions hosted by clinopyroxene D55R3B-min3, two melt inclusions D55R3B-min3-mi2 and D55R3B-min3-mi3 are assigned to Cluster 1 and a melt inclusion D55R3B-min3-mi5 is assigned to Cluster 2b (Figs. 12e and 14d; Table 1). Other two melt inclusions hosted in the same host clinopyroxene (D55R3B-min3) are D55R3B-min3-mi4 (Cluster 1) and D55R3B-min3-mi6 (Cluster 2b) (Table 1). The clinopyroxene D55R3B-min3 accommodates both Clusters 1 and 2b melt inclusions. Cluster 1 melt inclusions are hosted by high-Fe clinopyroxene whereas Cluster 2b melt inclusions are hosted by middle-Fe clinopyroxene, as described previously (Fig. 9d). These observations imply (i)

mixing of Clusters 1 and 2b melts in magma chambers, (ii) assimilation of brine into mixed melts, and (iii) crystallisation of clinopyroxene D55R3B-min3 from this mixed, brine-assimilated magma.

Characteristics of clusters from a volatiles perspective

The primary melts of Cluster 1 melt inclusions can be enriched in H_2O (≥ 6–7 wt %) and S (≥ 2000–3000 ppm) inferred from high content of H_2O (6–7 wt %) and S (2000–3000 ppm) in some Cluster 1 basaltic melt inclusions (Figs. 12a and b). Cluster 2b melt inclusions contain lower H_2O (2–3 wt %) and lower S (<1000 ppm) than Cluster 1 melt inclusions (Figs. 12a and b), suggesting that the H_2O and S content of the primary melts corresponding to Cluster 2 may be lower than those of Cluster 1. Experimental studies have shown that H_2O-rich and H_2O-poor primitive melts control magmatic differentiation along a calc-alkaline or tholeiitic differentiation trend (e.g. Hamada & Fujii, 2008; Tatsumi & Suzuki, 2009; Zimmer *et al.*, 2010). However, these experimental constraints are in contrast with our observations from Cluster 1 (tholeiitic affinity and possibly H_2O-rich primary melt) and Cluster 2b (calc-alkaline affinity and possibly H_2O-poor primary melt) melt inclusions. We infer that Cluster 1 melt inclusions form a tholeiitic differentiation trend because H_2O is effectively lost from the melt during

differentiation (Fig. 12a). Cluster 2b melt inclusions form a calc-alkaline differentiation trend, although they have a lower H_2O content than Cluster 1 melt inclusions. Thus, other factors than the differentiation of a H_2O-rich primitive melts may explain the origin of calc-alkaline Cluster 2 melt inclusions, which may include slab melting and/or crustal assimilation (e.g. Francis *et al*., 1980; Yogodzinski *et al.*, 1995; Benito *et al*., 1999).

The F and Cl content of Cluster 3b melt inclusions (both high-H_2O and low-H_2O subgroups) is lower than those in Clusters 1 and 2b melt inclusions (Figs. 12d and e). The lower F and Cl content is consistent with our inference that the mantle source of Clusters 3b melt inclusions is more depleted in incompatible elements. Partial melting of such a depleted and possibly refractory mantle source may be possible through the addition of slab-derived fluids (e.g. Pearce *et al*., 1992b; Morishita *et al*., 2011).

Cluster 4b melt inclusions are characterised by the highest F content reported in our study (Fig. 12d). The F content linearly correlates with K_2O ($\leq$1.5 wt %) but deviates from this correlation when $K_2O \geq 1.5$ wt %. In addition, the F/P ratio of Cluster 4b melt inclusions increases at $SiO_2 \geq 70$ wt % (Fig. 12f). The deviation of F and subsequent increase in F/P may result from the crystallisation of F-bearing apatite (e.g. Green & Watson, 1982) and is consistent with our petrographic observations. Indeed, apatite occurs as mineral inclusions in clinopyroxene in silicic core samples (e.g. U1438E-50R,

~40 Ma; Fig. 3d).

Characteristics of clusters from an igneous petrology perspective

In addition to geochemical constraints, the conditions under which each cluster was formed can also be evaluated from the perspective of igneous petrology. Pearce element ratio plots can be used to interpret basaltic suites that experienced various degrees of magmatic differentiation (e.g. Pearce, 1968; Ernst *et al*., 1988; Russell & Nicholls, 1988). Among the proposed Pearce-element ratio plots, an Al/K versus (2Ca+Na)/K plot was applied to the mafic melt inclusions assigned to Clusters 1, 2b and 3b (Fig. 15a). Clusters 1, 2b and 3b (low-H_2O subgroup) melt inclusions show an identical trend, implying that the geochemical variation of these melt inclusions can be explained by the crystallisation of clinopyroxene and plagioclase—a result not surprising given that our melt inclusions are hosted in these minerals. Melt inclusions assigned to Cluster 3b (high-H_2O subgroup) are offset from the main trend (Fig. 15a). Clinopyroxene and plagioclase crystallise synchronously in the low-H_2O melts (Fig. 15b), resulting in approximately constant Al_2O_3 with increasing SiO_2. In the case of the high-H_2O melts (Fig. 15b), clinopyroxene crystallises first (increasing Al_2O_3 with increasing SiO_2), to be followed later (at ~50 wt % SiO_2) by the crystallisation of plagioclase (decreasing Al_2O_3 with

increasing SiO_2), because the onset of plagioclase crystallisation is suppressed under H_2O-rich conditions (Figs. 15a and c).

Brandl *et al*. (2017) analysed melt inclusions hosted in clinopyroxene and plagioclase and did not find olivine in any of the core samples from Unit III. However, this does not necessarily mean that olivine did not crystallise from the corresponding parental melts at all, because olivine is easily altered by seawater and/or hydrothermal fluids (e.g. Pokrovsky & Schott, 2000; Ueda *et al*., 2017) and therefore may not be preserved in volcaniclastic sediments deposited at the seafloor. We assume that olivine crystallised from mafic melts, in addition to clinopyroxene and plagioclase. This assumption is necessary to apply projection of melts saturated with olivine + clinopyroxene + plagioclase in the basalt tetrahedron as a geobarometer (e.g. Walker *et al*., 1979; Grove & Bryan, 1983; Grove & Baker, 1984; Baker & Eggler, 1987). The normative composition of melt inclusions was calculated following the procedures of Tormey *et al.* (1987) and Grove (1993) and projected from the plagioclase apex, with olivine + clinopyroxene + plagioclase cotectics at 0.1 MPa (Walker *et al.*, 1979) and 200 MPa (Berndt *et al.*, 2005) and with orthopyroxene + clinopyroxene + plagioclase cotectics at 400 MPa (Hamada & Fujii, 2008) as pressure references (Fig. 16). A caveat is that a post-entrapment overgrowth of host clinopyroxene could slightly shift the projected

position of melt inclusions off the clinopyroxene (CPX) apex, resulting in apparently higher pressure. Clusters 1 and 2b melt inclusions are projected between pressure references of 0.1 and 200 MPa (Figs. 20a and b). Two levels are identified regarding Cluster 3b melt inclusions: lower pressures (0.1−200 MPa) for the low-H_2O subgroup and higher pressures (200−400 MPa) for the high-H_2O subgroup (Fig. 16c). Considering the experimental constraint that clinopyroxene crystallises earlier than plagioclase from hydrous basaltic melt at pressure conditions corresponding to middle to lower crust (≥ 300 MPa; Hamada & Fujii, 2008), it is reasonable to attribute the distinction between the low- and high-H_2O subgroups of Cluster 3b to a crystallisation differentiation under lower (0.1−200 MPa) and higher (~400 MPa) pressures, respectively. We argue that (1) a new magma chamber was formed at shallower levels as the magma-plumbing system evolved (e.g. Ushioda *et al.*, 2018) and therefore several magma chambers at different depths in the crust may have been present; (2) the melt was saturated with H_2O as most arc melts are (e.g. Plank *et al.*, 2013; 2−6 wt %); and (3) the saturated-H_2O content of Cluster 3b melts decreased with decreasing pressures (e.g. Hamada *et al.*, 2011, 2014). There seems to be no systematic difference in the pressure conditions under which crystallisation differentiation proceeded (0.1−200 MPa) among Clusters 1, 2b and 3b (low-H_2O subgroup) melt inclusions (Fig. 16).

Origin of each cluster constrained by thermodynamic modelling

Clusters 1, 2b, 3b (low-H_2O subgroup) and 3b (high-H_2O subgroup) are composed of larger numbers of melt inclusions when compared with other clusters, and range in composition from basalt to andesite as a result of crystallisation differentiation. Here, using thermodynamic modelling, we test whether geochemical variation of these four clusters can be explained solely by crystallisation differentiation. Among the thermodynamic models designated to simulate crystallisation differentiation, we use COMAGMAT 3.72 (e.g., Ariskin *et al.*, 1993; Ariskin 1999; Ariskin & Barmina, 2004), because it simulates crystallisation differentiation of hydrous arc magmas more reliably than MELTS (e.g., Almeev *et al*., 2004; Hamada, 2006; Kimura & Ariskin, 2014). COMAGMAT 3.72 is based on the two-lattice melt model, a kind of sub-ideal solution model after Bottinga & Weill (1972), Drake (1976) and Nielsen & Drake (1979), combined with a series of experimentally determined, mineral-melt geothermometers with empirical terms to compensate for the non-ideality of silicate melts. When simulating crystallisation differentiation using COMAGMAT 3.72, the starting conditions must be given *a priori*, and we performed forward simulation of "fractional crystallisation" starting from the most undifferentiated melt in each cluster. After

performing multiple simulations, we found that geochemical variation of Cluster 1 melt inclusions can be reproduced from their most undifferentiated melt with 2 wt % H_2O (U1438E-27R5W56-I11) at a pressure of 50 MPa (Fig. 17). This pressure condition is in agreement with the estimated pressure range (0.1–200 MPa; Fig. 16a), and the H_2O content agrees with the analytical results of H_2O measurements in most of our melt inclusions (2–3 wt %) (Fig. 12a). Variation in Al_2O_3 (Fig. 17b), which is not reproduced perfectly, can be explained by changes in initial H_2O content (0–2 wt %). Oxygen fugacity (f_{O2}) is the main control on the stability field of magnetite, the crystallisation of which affects the TiO_2 and FeO_t content of the evolving melts. Thus, we performed our simulations at variable oxygen fugacities of $\log f_{O2}$ equal to 0, +1 and +2 relative to the nickel-nickel oxide (NNO) buffer and found that $\log f_{O2}$ = +1 NNO best reproduces the geochemical variation of Cluster 1 melt inclusions (Fig. 17).

In a similar manner, the geochemical variation of Cluster 2b melt inclusions can be explained by crystallisation differentiation at P = 50 MPa from their most undifferentiated melt with 2.0 wt % H_2O (U1438D-60R4-I1; Fig. 18). These pressure and H_2O conditions are in agreement with the estimated pressure range (0.1–200 MPa; Fig. 16b) and analytical results of H_2O in melt inclusions (2–3 wt %; Fig. 12a). Variation in Al_2O_3 (Fig. 18b) can be reproduced by changing the initial H_2O content (0–2 wt %).

Trends in K_2O are not perfectly reproduced (Fig. 18g), probably because the initial K_2O content was set too high. A more oxidising condition ($\log f_{O2}$ = +1 to +2 NNO) than that of Cluster 1 likely reproduces geochemical variation of Cluster 2b melt inclusions (Fig. 18). We previously suggested that the calc-alkaline differentiation trend of Cluster 2b may be explained by slab melting and/or crustal assimilation. Here, however, we demonstrate that the tholeiitic differentiation trend of Cluster 1 and the calc-alkaline differentiation trend of Cluster 2b may result from relatively lower and higher f_{O2} conditions, respectively (e.g., Hamada & Fujii, 2008).

The origin of Cluster 3b should be discussed with respect to the H_2O content of the individual subgroups. The low-H_2O subgroup can be explained by crystallisation differentiation at P = 50 MPa from their most undifferentiated melt with 2.0 wt % H_2O (U1438D-63R1W-I6; Fig. 19) at $\log f_{O2}$ = +1 NNO. The Cluster 4a melt inclusion, which extends from the geochemical range of Cluster 3b melt inclusions towards higher SiO_2 content, can be reproduced by crystallisation differentiation from the undifferentiated Cluster 3b melt inclusions (low-H_2O subgroup) (Fig. 19). This argument is consistent with similar trace element patterns observed in Clusters 3b and 4a melt inclusions (Fig. 13c). Trends in TiO_2 (Fig. 19a) and K_2O (Fig. 19g) are not perfectly reproduced, probably because the initial TiO_2 and K_2O content was set too high. The small numbers of melt

inclusions assigned to the high-H_2O subgroup make a thorough evaluation difficult. However, they can be reproduced at P = 300 MPa and by assuming an initial H_2O of 6 wt % (D55R3A-min8-mi4; Fig. 20) and are thus in agreement with our previous pressure estimates and H_2O analyses. The geochemical variation of Cluster 3b melt inclusions (high-H_2O subgroup) is best reproduced at log f_{O2} = NNO.

The magmatic processes producing the geochemical variations observed in each cluster are likely to be more complex (e.g., crystallisation differentiation following magma ascent and degassing) than the constant conditions assumed in this thermodynamic modelling. However, the overall geochemical variation of melt inclusions assigned to each cluster can be broadly reproduced by crystallisation differentiation assuming constant pressure P = 50 MPa (~2-km deep) and ~2 wt % H_2O (almost saturated H_2O content at 50 MPa) for Clusters 1, 2b and 3b (low-H_2O subgroup) melt inclusions, and assuming constant pressure P = 300 MPa (~15-km deep) and ~6 wt % H_2O (almost saturated H_2O content at 300 MPa) for Cluster 3b (high-H_2O subgroup) melt inclusions. We infer that proto-IBM arc magmas underwent polybaric crystallisation differentiation under H_2O-saturated conditions, as discussed in the petrological study of the Izu-Oshima volcano, present-day IBM arc (e.g. Hamada *et al*., 2011, 2014).

New insights based on Site U1438 melt inclusion study

Brandl *et al*. (2017) concluded the following: (1) the volcanism of depleted calc-alkaline affinity shifted gradually to enriched tholeiitic affinity with time (30−40 Ma); and (2) such a compositional shift is linked to both the volcanic productivity, as expressed by deposition rates of volcanic sediments, and the maturation of an evolving island arc. As an extended study of Brandl *et al.* (2017), this study separated the geochemical dataset of melt inclusions into five statistically robust clusters which can be further separated into a total of eight subclusters, and their origins were discussed. We separated the "calc-alkaline affinity" of Brandl *et al*. (2017) into two distinct clusters: a cluster of medium-K calc-alkaline melt inclusions (Cluster 2b) and another cluster of low-K calc-alkaline melt inclusions (Cluster 3b) representing geochemically enriched and depleted mantle sources, respectively.

We have demonstrated that (1) the eruption of depleted low-K calc-alkaline magmas (Cluster 3b) occurred prior to 40 Ma and ceased sharply at 35 Ma; (2) eruption of depleted low-K calc-alkaline magmas (Cluster 3b), enriched medium-K calc-alkaline magmas (Cluster 2b) and enriched medium-K tholeiitic magmas (Cluster 1) overlapped temporally between 35 and 38−39 Ma; and (3) the eruption of enriched medium-K tholeiitic and enriched depleted medium-K calc-alkaline magmas became predominant

thereafter (Figs. 10 and 11). Our findings thus present a different, more detailed overview of the temporal evolution of the proto-IBM arc volcanism when compared to Brandl *et al.* (2017).

Of particular interest is the question regarding the nature of the mantle source that generated depleted low-K calc-alkaline magmas (Cluster 3b) in the time period of 35−40 Ma. Previous modelling of rare-earth elements has shown that both tholeiitic and calc-alkaline arc basalts of the Ogasawara (Bonin) Islands (38–45 Ma) were generated by partial melting of fertile lherzolitic mantle more enriched than DMM (Figs. 13e–g; Kanayama *et al*., 2014; Umino *et al.*, 2015). This argument suggests that mantle convection was established soon after the beginning of the Pacific slab subduction at 52 Ma (e.g. Arculus *et al*., 2015a; Reagan *et al*., 2017) and replaced the depleted residual mantle after extraction of proto-arc basalts by more fertile mantle through convection by 45 Ma. Such mantle convection was induced by the drag force of the subducting slab lithosphere and was accompanied by mantle upwelling as counter flow from the deeper rear-arc regions (e.g. Iwamori, 1998). Mantle convection has been an essential driving force to activate the arc volcanism of the IBM arc and the geochemical evolution of the source mantle (e.g. Straub *et al.*, 2010). The volcanism of the proto-IBM arc shifted from the eruption of boninites on the Chichijima-Mukojima-Guam (44−48 Ma) to the eruption

of arc magmas on Hahajima Island and the western scarp of the Bonin Ridge (38–45 Ma; Ishizuka *et al*., 2006, 2011a; Kanayama *et al*., 2014; Umino *et al.*, 2015). Arc volcanism along the KPR followed (25–49 Ma; Ishizuka *et al.*, 2011b, 2018), on which we have focused in this study. Cluster 3b melt inclusions (35−40 Ma; Fig. 13c) are less depleted than boninites (Fig. 13g), and we thus infer that the mantle source of Cluster 3b melt inclusions may reflect the residue of proto-arc basalts at the rear-arc side (Reagan *et al.*, 2017). High H_2O content (6–7 wt %) in some Cluster 3b melt inclusions (high-H_2O subgroup) is consistent with the idea of partial melting of a depleted and possibly refractory mantle source through the addition of slab-derived fluids to generate primary Cluster 3b melts. Numerical simulation suggests that fluids derived from a subducted slab hydrate a limited area of overriding lithosphere at the shallower level when subduction initiates, and that dehydration reaches a steady state where the hydration of serpentine becomes predominant at deeper levels thereafter (Arcay *et al*., 2005). The high H_2O content in some Cluster 3b melt inclusions may be explained by a focused release of slab-derived fluids following subduction initiation at 52 Ma. We infer that the rocks with enriched medium-K tholeiitic (Cluster 1) and enriched medium-K calc-alkaline affinities (Cluster 2b) represent differentiated rock series from primary melts generated by partial melting of replenished, more enriched mantle sources. We also infer that slight

differences in oxygen fugacities of such primary melts resulted in the formation of coeval tholeiitic and calc-alkaline affinities, as discussed in this study based on thermodynamic modelling.

CONCLUSIONS

IODP Expedition 351 recovered volcaniclastic sediments from Site U1438 that represent a continuous record of the magmatic evolution of the proto-IBM arc between 30 and 40 Ma. We analysed volatiles (H_2O, S, F and Cl) and P_2O_5 for 47 selected melt inclusions (>20 μm) with SIMS and performed statistical analysis on the major element composition of 237 representative melt inclusions from Unit III of Hole U1438 (30−40 Ma; Brandl *et al*., 2017). We statistically distinguished five main clusters, which can be further separated into a total of eight subclusters by considering their trace and volatile element compositions. The Cluster 1 melt inclusions (n = 84; 30−38 Ma) are enriched medium-K melts, which form a tholeiitic differentiation trend. Some melt inclusions are characterised by relatively high S content (≥1000 ppm). The Cluster 2 melt inclusions (n = 61) can be divided into two individual subclusters; Clusters 2a (n = 2) and 2b (n = 59). The Cluster 2b melt inclusions (30−39 Ma) are enriched medium-K calc-alkaline melts. The Cluster 3 melt inclusions (n = 67) can be divided into two individual subclusters;

Clusters 3a (n = 2) and 3b (n = 65). The Cluster 3b melt inclusions (n = 65) are depleted low-K calc-alkaline melts, which can be generated by partial melting of a depleted mantle source. The Cluster 3b melt inclusions (35−40 Ma) can be further divided into high-H_2O and low-H_2O subgroups, reflecting the crystallisation differentiation of H_2O-saturated melts at deeper and shallower crustal levels, respectively. Cluster 4 melt inclusions (n = 22) are dacitic and rhyolitic melts, which form a calc-alkaline trend. Cluster 5 melt inclusions (n = 3) are medium-K melts characterised by low P_2O_5. We have demonstrated that (1) the eruption of depleted low-K calc-alkaline magmas (Cluster 3b) occurred from >40 Ma and ceased sharply at 35 Ma; (2) the eruption of depleted low-K calc-alkaline magmas (Cluster 3b), enriched medium-K calc-alkaline magmas (Cluster 2b) and enriched medium-K tholeiitic magmas (Cluster 1) overlapped temporally between 35 and 38−39 Ma; and (3) the eruption of enriched medium-K tholeiitic magmas (Cluster 1) and enriched medium-K calc-alkaline magmas (Cluster 2b) became predominant thereafter. Such temporal evolution of the proto-IBM arc volcanism reflects a replenishment of enriched mantle into depleted mantle through convection. Identification of such distinct magma types becomes possible by (1) using drilled core samples from the deep sea of the rear-arc side, because no corresponding geological record of the proto-IBM rear-arc volcanism has been recovered to date; and (2) applying statistical analysis on

multivariable major element composition of melt inclusions and interpreting the findings combined with their trace and volatile element compositions. Thermodynamic modelling indicates that the overall geochemical variation of melt inclusions assigned to each cluster can be broadly reproduced by crystallisation differentiation assuming P = 50 MPa (~2 km deep) and ~2 wt % H_2O (almost saturated H_2O content at 50 MPa) for Clusters 1, 2b and 3b (low-H_2O subgroup) melt inclusions, and assuming P = 300 MPa (~15 km deep) and ~6 wt % H_2O (almost saturated H_2O content at 300 MPa) for Cluster 3b (high-H_2O subgroup) melt inclusions. The estimated H_2O content (~2 wt % or ~6 wt %) is consistent with the analytical results of volatile elements in melt inclusions with SIMS. Assuming an oxygen fugacity (f_{O2}) of $\log f_{O2}$ equal to +1 relative to the nickel-nickel oxide (NNO) buffer best reproduces the geochemical variation of melt inclusions assigned to Clusters 1 and 2b, but assuming a more oxidising condition ($\log f_{O2}$ = +1 to +2 NNO) likely reproduces geochemical variation of Cluster 3b melt inclusions (low-H_2O subgroup). We infer that slight differences in oxygen fugacities resulted in the formation of coeval tholeiitic and calc-alkaline affinities.

Acknowledgement

This study used samples provided by the IODP. The authors would like to thank

the crew of the D/V JOIDES Resolution for the safe operation of the expedition, and all the scientists and technical staff participating in Expedition 351. MH benefited from the Japan Drilling Earth Science Consortium (J-DESC) for supporting his participation on Expedition 351 and its related meetings, and the JAMSTEC Library for its dedicated service to collect relevant literature. MH also thank Y. Tamura, J.-I. Kimura, S. M. Straub for their fruitful discussions, and T. Hanyu and K. Tani for their support with sample preparation. PAB thanks the Alexander von Humboldt Foundation for funding his Feodor Lynen Research Fellowship and R. J. Arculus and H. St.C. O'Neill for the welcoming atmosphere at the Research School of Earth Sciences of ANU, Canberra. IPS acknowledges the UK-IODP program and the NERC (grant NE/M007782/1) for his participation in Expedition 351 and UK-IODP and NERC 'Mantle Volatiles' consortia for post-cruise research support. Finally the authors offers special thanks to S. Umino and anonymous reviewers for their thoughtful reviews and many constructive comments, and G. Zellmer and M. Wilson for their effort to handle this manuscript.

References

Aitchison, J. (1982) The statistical analysis of compositional data (with discussion). *Journal of the Royal Statistical Society, Series B (Statistical Methodology)* **44**, 139-177.

Aitchison, J. (1984) The statistical analysis of geochemical compositions. *Mathematical Geology* **16**, 531-564.

Aitchison, J. (1986) The statistical analysis of compositional data. Chapman & Hall Ltd., London. Reprinted (2003) with additional material by The Blackburn Press, Caldwell, NJ, USA.

Allègre, C. J., Hamelin, B., Provost, A. & Dupré, B. (1987) Topology in isotopic multispace and origin of the mantle chemical heterogeneities. *Earth and Planetary Science Letters* **81**, 319-337.

Almeev, R. R., Ariskin, A. A. & Pletchov, P. Yu. (2004) Calculations of mineral-melt equilibria in tholeiitic system: MELTS versus COMAGMAT. *Lithos* **73**, S1.

Arcay, D., Tric, E. & Doin, M.-P. (2005) Numerical simulations of subduction zones: Effect of slab dehydration on the mantle wedge dynamics. *Physics of the earth and Planetary Interiors* **149**, 133-153.

Arculus, R. J., Gill, J. B., Cambray, H., Chen, W. & Stern, R. J. (1995) Geochemical evolution of arc systems in the Western Pacific: The ash and turbidite record recovered by drilling. In: Taylor, B. & Natland, J. (eds) *Active margins and marginal basins of the Western Pacific. Geophysical Monograph* **88**, 45-65.

Arculus, R. J., Ishizuka, O., Bogus, K. A., Gurnis, M., Hickey-Vargas, R., Aljahdali, M. H., Bandini-Maeder, A. N., Barth, A. P., Brandl, P. A., Drab, L., do Monte Guerra, R., Hamada, M., Jiang, F., Kanayama, K., Kender, S., Kusano, Y., Li, H., Loudin, L. C., Maffione, M., Marsaglia, K. M., McCarthy, A., Meffre, S., Morris, A., Neuhaus, M., Savov, I. P., Sena, C., Tepley, F. J. III, van der Land, C., Yogodzinski, G. M. & Zhang, Z. (2015a) A record of spontaneous subduction initiation in the Izu–Bonin–Mariana arc. *Nature Geoscience* **8**, 728-733.

Arculus, R. J., Ishizuka, O., Bogus, K., Aljahdali, M. H., Bandini-Maeder, A. N., Barth, A. P., Brandl, P. A., do Monte Guerra, R., Drab, L., Gurnis, M. C., Hamada, M., Hickey-Vargas, R. L., Jiang, F., Kanayama, K., Kender, S., Kusano, Y., Li, H., Loudin, L. C., Maffione, M., Marsaglia, K. M., McCarthy, A., Meffre, S., Morris, A., Neuhaus, M., Savov, I. P., Sena Da Silva, C. A., Tepley, F. J. III, van der Land, C., Yogodzinski, G. M. & Zhang, Z. (2015b) Site U1438. In Arculus, R. J., Ishizuka, O., Bogus, K. & Expedition 351 Scientists (eds), Proceedings of the International Ocean Discovery Program, Volume 351 Izu–Bonin–Mariana Arc Origins, International Ocean Discovery Program. doi: 10.14379/iodp.proc.351.103.2015.

Ariskin, A. A. (1999) Phase equilibria modeling in igneous petrology: Use of COMAGMAT model for simulating fractionation of ferrobasaltic magmas and the genesis of high-alumina basalt. *Journal of Volcanology and Geothermal Research* **90**, 115-162.

Ariskin, A. A. & Barmina, G. S. (2004) COMAGMAT: Development of a magma crystallization model and its petrological applications. *Geochemistry International* **42**, S1-S157.

Ariskin, A. A., Frenkel, M. Y., Barmina, G. S. & Nielsen, R. L. (1993) COMAGMAT: A Fortran program to model magma differentiation processes. *Computers & Geosciences* **19**, 1155-1170.

Baker, D. R. & Eggler, D. H. (1987) Compositions of anhydrous and hydrous melts coexisting with plagioclase, augite, and olivine or low-Ca pyroxene from 1 atm to 8 kbar: Application to the Aleutian volcanic center of Atka. *American Mineralogist* **72**, 12-28.

Barth, A. P., Tani, K., Meffre, S., Wooden, J. L., Coble, M. A., Arculus, R. J., Ishizuka, O. & Shukle, J. T. (2017) Generation of silicic melts in the early Izu–Bonin arc recorded by detrital zircons in proximal arc volcaniclasitc rocks from the Philippine Sea. *Geochemistry, Geophysics, Geosystems* **18**, 3576-3591. https://doi.org/10.1002/2017GC006948

Benito, R., López-Ruiz, J., Cebriá, J. M., Hertogen, J., Doblas, M., Oyarzun, R. & Demaiffe, D. (1999) Sr and O isotope constraints on source and crustal contamination in the high-K calc-alkaline and shoshonitic Neogene volcanic rocks of SE Spain. *Lithos* **46**,

773-802.

Berndt, J., Koepke, J. & Holtz, F. (2005) An experimental investigation of the influence of water and oxygen fugacity on differentiation of MORB at 200 MPa. *Journal of Petrology* **46**, 135-167.

Bottinga, Y. & Weill, D. F. (1972) The viscosity of magmatic silicate liquids: a model for calculation. *American Journal of Science* **272**, 438-475.

Brandl, P. A., Hamada, M., Arculus, R. J., Johnson, K., Marsaglia, K. M., Savov, I. P., Ishizuka, O. & Li, H. (2017) The arc arises: The links between volcanic output, arc evolution and melt composition. *Earth and Planetary Science Letters* **461**:73-84.

Brandmeier, M. & Wörner, G. (2016) Compositional variations of ignimbrite magmas in the Central Andes over the past 26 Ma—A multivariate statistical perspective. *Lithos* **262**, 713-728.

Busby, C. J., Tamura, Y., Blum, P., Guèrin, G., Andrews, G. D. M., Barker, A. K., Berger, J. L. R., Bongiolo, E. M., Bordiga, M., DeBari, S. M., Gill, J. B., Hamelin, C., Jia, J., John, E. H., Jonas, A.-S., Jutzeler, M., Kars, M. A. C., Kita, Z. A., Konrad, K., Mahony, S. H., Martini, M., Miyazaki, T., Musgrave, R. J., Nascimento, D. B., Nichols, A. R. L., Ribeiro, J. M., Sato, T., Schindlbeck, J. C., Schmitt, A. K., Straub, S. M., Mleneck-Vautravers, M. J. & Yang, A. Y. (2017) The missing half of the subduction factory: shipboard results from the Izu rear arc, IODP Expedition 350. *International Geology Review*, doi: 10.1080/00206814.2017.1292469

Coombs, M. L., Sisson, T. W. & Kimura, J. -I. (2004) Ultra-high chlorine in submarine Kīlauea glasses: evidence for direct assimilation of brine by magma. *Earth and Planetary Science Letters* **217**, 297-313.

Drake, M. J. (1976) Plagioclase-melt equilibria. *Geochimica et Cosmochimica Acta* **40**, 457-466.

Druitt, T. H., Mercier, M., Florentin, L., Deloule, E., Cluzel, N., Flaherty, T., Médard, E. & Cadoux, A. (2016) Magma storage and extraction associated with Plinian and interplinian activity at Santorini caldera (Greece). *Journal of Petrology* **57**, 461-494.

Ernst, R. E., Fowler, A. D. & Pearce, T. H. (1988) Modelling of igneous fractionation and other processes using Pearce diagrams. *Contributions to Mineralogy and Petrology* **100**, 12-18.

Francis, P. W., Thorpe, R. S., Moorbath, S., Kretzschmar, G. A. & Hammill, M. (1980) Strontium isotope evidence for crustal contamination of calc-alkaline volcanic rocks from Cerro Galan, northwest Argentina. *Earth and Planetary Science Letters* **48**, 257-267.

Fryer, P., Mottl, M., Johnson, L., Haggerty, J., Phipps, S. & Maekawa, H. (1995) Serpentine bodies in the forearcs of western Pacific convergent margins: Origin and associated fluids. In: Taylor, B & Natland, J. (eds) *Active Margins and Marginal Basins of the Western Pacific*. Geophysical Monograph **88**, American Geophysical Union, pp. 259-279.

Fryer, P. B., Wheat, C. G., Williams, T., Albers, E. J., Bekins, B., Magalhaes, V., Debret, B. P. R., Deng, J., Dong, Y., Eickenbusch, P., Frery, E. A., Ichiyama, Y., Johnson, K., Johnson, R. M., Kevorkian, R. T., Kurz, W., Mantovanelli, S. S., Menapace, W., Menzies, C. D., Michibayashi, K., Moyer, C. L., Mullane, K. K., Park, J.-W., Price, R. E., Ryan, J. G., Shervais, J. W., Sissmann, O. J., Suzuki, S., Takai, K., Walter, B., Zhang, R. & Zhang, R. (2017) Expedition 366 Preliminary Report: Mariana Convergent Margin and South Chamorro Seamount, International Ocean Discovery Program. https://doi.org/10.14379/iodp.pr.366.2017.

Gill, J. B. (1981) Orogenic Andesites and Plate Tectonics. Springer-Verlag, 390 pp.

Green, T. H. & Watson, E. B. (1982) Crystallization of apatite in natural magmas under high pressure, hydrous conditions, with particular reference to 'orogenic' rock series. *Contributions to Mineralogy and Petrology* **79**, 96-105.

Grove, T. L. (1993) Corrections to expressions for calculating mineral compositions in "Origin of calc-alkaline series lavas at Medicine Lake volcano by fractionation, assimilation and mixing" and "Experimental petrology of normal MORB near Kane Fracture Zone: 22º–25 ºN, mid-Atlantic ridge". *Contributions to Mineralogy and Petrology* **114**, 422-424.

Grove, T. L. & Baker, M. B. (1984) Phase equilibrium controls on the tholeiitic versus calc-alkaline differentiation trends. *Journal of Geophysical Research* **89**, 3253-3274.

Grove, T. L. & Bryan, W. B. (1983) Fractionation of pyroxene-phyric MORB at low pressure: An experimental study. *Contributions to Mineralogy and Petrology* **84**, 293-309.

Hamada, M. (2006) Experimental study on the differentiation of island arc basalt. Ph. D. Dissertation, The University of Tokyo, 143 pp.

Hamada, M. & Fujii, T. (2008) Experimental constraints on the effects of pressure and H_2O on the fractional crystallization of high-Mg island arc basalt. *Contributions to Mineralogy and Petrology* **155**, 767-790.

Hamada, M., Kawamoto, T., Takahashi, E. & Fujii, T. (2011) Polybaric degassing of island arc low-K tholeiitic basalt magma recorded by OH concentrations in Ca-rich plagioclase. *Earth and Planetary Science Letters* **308**, 259-266.

Hamada, M., Okayama, Y., Kaneko, T., Yasuda, A & Fujii, T. (2014) Polybaric crystallization differentiation of H_2O-saturated island arc low-K tholeiite magmas: a case study of the Izu–Oshima volcano in the Izu arc. *Earth, Planets and Space* **66**:15.

Hart, S. R., Hauri, E. H., Oschmann, L. A. & Whiteland, J. A. (1992) Mantle plumes and entrainment: isotopic evidence. *Science* **256**, 517-520.

Hauri, E., Wang, J., Dixon, J. E., King, P. L., Mandeville, C. & Newman, S. (2002) SIMS analysis of volatiles in silicate glasses 1. Calibration, matrix effects and comparisons with FTIR. *Chemical Geology* **183**, 99-114.

Hickey-Vargas, R., Savov, I. P., Bizimis, M., Ishii, T. & Fujioka, K. (2006) Origin of diverse geochemical signatures in igneous rocks from the West Philippine Basin: implications for tectonic models. In: Back-arc spreading systems: Geological, Biological, Chemical, and Physical Interactions, Christie, D., Fisher, C. R., Lee, S. -M. & Givens, S. (eds), *Geophysical Monograph* **166**, 287-303.

Hickey-Vargas, R., Yogodzinski, G. M., Ishizuka, O., McCarthy, A., Bizimis, M.,

Kusano, Y., Savov, I. P. & Arculus, R. (2018) Origin of depleted basalts during subduction initiation and early development of the Izu-Bonin-Mariana island arc: Evidence from IODP expedition 351 site U1438, Amami-Sankaku basin, *Geochimica et Cosmochimica Acta* **229**, 85-111.

Ishizuka, O., Kimura, J. -I., Li, Y. -B., Stern, R. J., Reagan, M. K., Taylor, R. N., Ohara, Y., Bloomer, S. H., Ishii, T., Hargrove, U. S. III & Haraguchi, S. (2006) Early stages in the evolution of Izu–Bonin arc volcanism: New age, chemical, and isotopic constraints. *Earth and Planetary Science Letters* **250**, 385-401.

Ishizuka, O., Tani, K., Reagan, M. K., Kanayama, K., Umino, S., Harigane, Y., Sakamoto, I., Miyajima, Y., Yuasa, M. & Dunkley, D. J. (2011a) The timescales of subduction initiation and subsequent evolution of an oceanic island arc. *Earth and Planetary Science Letters* **306**, 229-240.

Ishizuka, O., Taylor, R. N., Yuasa, M. & Ohara, Y. (2011b) Making and breaking an island arc: A new perspective from the Oligocene Kyushu–Palau arc, Philippine Sea. *Geochemistry Geophysics Geosystems* **12**:Q05005.

Ishizuka, O., Tani, K. & Reagan, M. K. (2014a) Izu–Bonin–Mariana forearc crust as a modern ophiolite analogue. *Elements* **10**, 115-120.

Ishizuka, O., Umino, S., Taylor, R. N. & Kanayama, K. (2014b) Evidence for hydrothermal activity in the Earliest Stages of Intraoceanic Arc Formation: Implications for ophiolite-hosted hydrothermal activity. *Economic Geology* **109**, 2159-2177.

Ishizuka, O., Hickey-Vargas, R., Arculus, R. J., Yogodzinski, G. M., Savov, I. P., Kusano, Y., McCarthy, A., Brandl, P. A. & Sudo, M. (2018) Age of Izu–Bonin–Mariana arc basement. *Earth and Planetary Science Letters* **481**, 80-90.

Iwamori, H. (1998) Transportation of H_2O and melting in subduction zones. *Earth and Planetary Science Letters* **160**, 65-80.

Iwamori, H. & Albarède, F. (2008) Decoupled isotopic record of ridge and subduction zone processes in oceanic basalts by independent component analysis. *Geochemistry, Geophysics, Geosystems* **9**, Q04033.

Iwamori, H. & Nakamura, H. (2012) East-west mantle geochemical hemispheres constrained from Independent Component Analysis of basalt isotopic compositions. *Geochemical Journal* **46**, e39-e-46.

Iwamori, H. & Nakamura, H. (2015) Isotopic heterogeneity of oceanic, arc and continental basalts and its implications for mantle dynamics. *Gondwana Research* **27**, 1131-1152.

Iwamori, H., Yoshida, K., Nakamura, H., Kuwatani, T., Hamada, M., Haraguchi, S. & Ueki, K. (2017) Classification of geochemical data based on multivariate statistical analyses: complementary roles of clustering, principal component and independent component analyses. *Geochemistry, Geophysics, Geosystems* **18**, doi: 10.1002/2016GC006663.

Jochum, K. P., Dingwell, D. B., Rocholl, A., Stoll, B., Hofmann, A. W., Becker, S., Besmehn, A., Bessette, D., Dietze, H. -J., Dulski, P., Erzinger, J., Hellebrand, E., Hoppe, P., Horn, I., Janssens, K., Jenner, G. A., Klein, M., McDonough, W. F., Maetz, M., Mezger, K., Münker, C., Nikogosian, I. K., Pickhardt, C., Raczek, I., Rhede, D., Seufert, H. M., Simakin, S. G., Sobolev, A. V., Spettel, B., Straub, S., Vincze, L., Willianos, A., Weckwerth, G., Weyer, S., Wolf, D. and Zimmer, M. (2000) The preparation and preliminary characterization of eight geological MPI-DING reference glasses for in-situ microanalysis. *Geostandards Newsletter* **24**, 87-133.

Johnson, K., Waldman, R. & Marsaglia, K. M. (2017) Data report: sedimentary columns with facies and bedding for Units II-IV at IODP Site U1438. In Arculus, R. J., Ishizuka, O., Bogus, K. & Expedition 351 Scientists (eds), Proceedings of the International Ocean Discovery Program, Volume 351 Izu–Bonin–Mariana Arc Origins, International Ocean Discovery Program. doi: 10.14379/iodp.proc.351.201.2017.

Kanayama, K., Umino, S. & Ishizuka, O. (2012) Eocene volcanism during the incipient stage of Izu–Ogasawara Arc: geology and petrology of the Mukojima Island Group, the Ogasawara Islands. *Island Arc* **21**, 288-316.

Kanayama, K., Umino, S. & Ishizuka, O. (2014) Shallow submarine volcano group in the early stage of island arc development: Geology and petrology of small islands south off

Hahajima main island, the Ogasawara Islands. *Journal of Asian Earth Sciences* **85**, 1-25.

Kimura, J.-I. & Ariskin, A. A. (2014) Calculation of water-bearing primary basalt and estimation of source mantle conditions beneath arcs: PRIMACALC2 model for WINDOWS. *Geochemistry, Geophysics, Geosystems* **15**, 1494-1514, doi: 10.1002/2014GC005329.

Kimura, J.-I., Nagahashi, Y., Satoguchi, Y. & Chang, Q. (2015) Origins of felsic magmas in Japanese subduction zone: Geochemical characteristics of tephra from caldera-forming eruptions <5 Ma. *Geochemistry, Geophysics, Geosystems* **16**, 2147-2174, doi: 10.1002/2015GC005854.

Kuwatani, T., Nagata, K., Okada, M., Watanabe, T., Ogawa, Y., Komai, T. & Tsuchiya, N. (2014) Machine-learning techniques for geochemical discrimination of 2011 Tohoku tsunami deposits. *Scientific Reports* **4**, 7077.

MacQueen, K. (1967) Some methods for classification and analysis of multivariate observations. In: Le Cam, L. M., Neyman, J. (eds) *Proceedings of the Fifth Berkeley Symposium on Mathematical Statistics and Probability, Berkeley, California* **1**, 281-297.

Michael, P. J. & Cornell, W. C. (1998) Influence of spreading rate and magma supply on crystallization and assimilation beneath mid-ocean ridges: Evidence from chlorine and major element chemistry of mid-ocean ridge basalts. *Journal of Geophysical Research* **103**, 18325-18356.

Miyashiro, A. (1974) Volcanic rock series in island arcs and active continental margins. *American Journal of Science* **274**, 321-355.

Morishita, T., Dilek, Y., Shallo, M., Tamura, A. & Arai, S. (2011) Insight into the upper mantle section of a maturing arc: The Eastern Mirdita ophiolite, Albania. *Lithos* **124**, 215-226.

Nakanishi, M., Tamaki, K. & Kobayashi, K. (1992) Magnetic anomaly lineations from Lake Jurassic to Early Cretaceous in the west-central Pacific Ocean. *Geophysical Journal International* **109**, 701-719, doi:10.1111/j.1365-246X.1992.tb00126.x.

Nielsen, R. L., Drake, M. J. (1979) Pyroxene-melt equilibria. *Geochimica et Cosmochimica Acta* **43**, 1259-1272.

Pearce, J. A., Thirlwall, M. F., Ingram, G., Murton, B. J., Arculus, R. J. & van der Laan, S. R. (1992a) Isotopic evidence for the origin of boninites and related rocks drilled in the Izu–Bonin (Ogasawara) forearc, Leg 125. In: Fryer, P., Pearce, J. A., Stokking L. B. *et al.* (eds) *Ocean Drilling Program Scientific Results, 125*. College Station, TX: Ocean Drilling Program, pp. 237-261.

Pearce, J. A., van der Laan, S. R., Arculus, R. J., Murton, B. J., Ishii, T., Peate, D. W. & Parkinson, I. J. (1992b) Boninite and harzburgite from Leg 125 (Bonin-Mariana-forearc): a case study of magma genesis during the initial stages of subduction. In: Fryer, P., Pearce, J. A., Stokking L. B. *et al.* (eds) *Ocean Drilling Program Scientific Results, 125*. College Station, TX: Ocean Drilling Program, pp. 623-659.

Pearce, T. H. (1968) A contribution to the theory of variation diagrams. *Contributions to Mineralogy and Petrology* **19**, 142-157.

Petrelli, M. & Perugini, D. (2016) Solving petrological problems through machine learning: the study case of tectonic discriminations using geochemical and isotopic data. *Contributions to Mineralogy and Petrology* **171**, 81.

Plank, T., Kelley, K. A., Zimmer, M. M., Hauri, E. H. & Wallace, P. J. (2013) Why do mafic arc magmas contain ~4 wt% water on average? *Earth and Planetary Science Letters* **364**, 168-179.

Pokrovsky, O. S. & Schott, J. (2000) Kinetics and mechanism of forsterite dissolution at 25℃ and pH from 1 to 12. *Geochimica et Cosmochimica Acta* **64**, 3313-3325.

Putirka, K. D. (2008) Thermometers and barometers for volcanic systems. *Reviews in Mineralogy & Geochemistry* **69**, 61-120.

Reagan, M. K., Hanan, B. B., Heizler, M. T., Hartman, B. S. & Hickey-Vargas, R. (2008) Petrogenesis of volcanic rocks from Saipan and Rota, Mariana Islands, and implications for the evolution of nascent island arcs. *Journal of Petrology* **49**, 441-464.

Reagan, M. K., Ishizuka, O., Stern, R. J., Kelly, K. A., Ohara, Y., Blichert–Toft, J., Bloomer, S. H., Cash, J., Fryer, P., Hanan, B. B., Hickey-Vargas, R., Ishii, T., Kimura, J.-I., Peate, D. W., Rowe, M. C. & Woods, M. (2010). Fore-arc basalts and subduction initiation in the Izu–Bonin–Mariana system. *Geochemistry, Geophysics, Geosystems* **11**, Q03X12, doi: 10.1029/2009GC002871.

Reagan, M. K., Pearce, J. A., Petronotis, K., Almeev, R. R., Avery, A. J., Carvallo, C., Chapman, T., Christeson, G. L., Ferrè, E. C., Godard, M., Heaton, D. E., Kirchenbaur, M., Kurz, W., Kutterolf, S., Li, H., Li, Y., Michibayashi, K., Morgan, S., Nelson, W. R., Prytulak, J., Python, M., Robertson, A. H. F., Ryan, J. G., Sager, W. W., Sakuyama , T., Shervais, J. W., Shimizu, K. & Whattam, S. A. (2017) Subduction initiation and ophiolite crust: new insights from IODP drilling. *International Geology Review* **59**, 1439-1450.

Reagan, M. K., Heaton, D. E., Schmitz, M. D., Pearce, J. A., Shervais, J. W. & Koppers, A. A. P. (2019) Forearc ages reveal extensive short-lived and rapid seafloor spreading following subduction initiation. *Earth and Planetary Science Letters* **506**, 520-529.

Russel, J. K. & Nicholls, J. (1988) Analysis of petrologic hypotheses with Pearce element ratios. *Contributions to Mineralogy and Petrology* **99**, 25-35.

Saal, A. E., Hauri, E. H., Langmuir, C. H. & Perfit, M. R. (2002) Vapour undersaturation in primitive mid-ocean-ridge basalt and the volatile content of Earth's upper mantle. *Nature* **419**, 451-455.

Savov, I. P., Hickey-Vergas, R., D'Antonio, M., Ryan, J. G. & Spadea, P. (2006) Petrology and geochemistry of West Philippine Basin basalts and early Palau-Kyushu arc volcanic clasts from ODP Leg 195, Site 1201D: Implications for the early history of the Izu–Bonin–Mariana arc. *Journal of Petrology* **47**, 277-299.

Shervais, J. W., Reagan, M., Haugen, E., Almeev, R., Pearce, J., Prytulak, J., Ryan, J. G., Whattam, S., Godard, M., Chapman, T., Li, H., Kurz, W., Nelson, W. R., Heaton, D., Kirchenbaur, M., Shimizu, K., Sakuyama, T., Li, Y. & Vetter, S. K. (2019) Magmatic response to subduction initiation, Part I: Forearc basalts of the Izu-Bonin arc from IODP Expedition 352. *Geochemistry, Geophysics, Geosystems*, doi: 10.1029/2018GC007731.

Shimizu, K., Shimizu, N., Komiya, T., Suzuki, K., Maruyama, S., & Tatsumi, Y. (2009).

CO_2-rich komatiitic melt inclusions in Cr-spinels within beach sand from Gorgona Island, Colombia. *Earth and Planetary Science Letters* **288**, 33-43.

Shimizu, K., Ushikubo, T., Hamada, M., Itoh, S., Higashi, Y., Takahashi, E. & Ito, M. (2017). H_2O, CO_2, F, S, Cl and P_2O_5 analyses of silicate glasses using SIMS: Report of volatile standard glasses. *Geochemical Journal* **51**, 299-313.

Shimizu, K., Ito, M., Chang, Q., Miyazaki, T., Ueki, K., Toyama, C., Senda, R., Vaglarov, B. S., Ishikawa, T. & Kimura, J.-I. (2019) Identifying volatile mantle trend with the water-fluorine-cerium systematics of basaltic glass. *Chemical Geology* **522**, 283-294.

Stern, R. J. (2002) Subduction zones. *Reviews of Geophysics* **40**:1012.

Stern, R. J. (2004) Subduction initiation: Spontaneous and induced. *Earth and Planetary Science Letters* **226**, 275-292.

Stern, R. J. & Bloomer, S. H. (1992) Subduction zone infancy: example from the Eocene Izu–Bonin–Mariana and Jurassic California Arcs. *Geological Society of America Bulletin* **104**, 1621-1636.

Stern, R. J., Fouch, M. J. & Klemperer, S. L. (2003) An overview of the Izu–Bonin–Mariana subduction factory. In: Eiler, J. M. (ed) *Inside the Subduction Factory. Geophysical Monograph* **138**, 175-222.

Stracke, A. (2012) Earth's heterogeneous mantle: A product of convection–driven interaction between crust and mantle. *Chemical Geology* **330-331**, 274-299.

Straub, S. M. & Layne, G. D. (2003a) Decoupling of fluids and fluid-mobile elements during shallow subduction: Evidence from halogen-rich andesite melt inclusions from the Izu arc volcanic front. *Geochemistry Geophysics Geosystems* **4**(7), 9003, doi: 10.1029/2002GC000349.

Straub, S. M. & Layne, G. D. (2003b) The systematics of chlorine, fluorine, and water in Izu arc front volcanic rocks: Implications for volatiles recycling in subduction zones. *Geochimica et Cosmochimica Acta* **67**, 4179-4203.

Straub, S. M., Goldstein, S. L., Cornelia, C., Schmidt, A. & Gomez-Tuena, A. (2010) Slab and mantle controls on the Sr-Nd-Pb-Hf isotope evolution of the post 42 Ma Izu-Bonin volcanic arc. *Journal of Petrology* **51**, 993-1026.

Straub, S. M., Woodhead, J. D. & Arculus, R. J. (2015) Temporal evolution of the Mariana arc: mantle wedge and subducted slab controls revealed with a tephra perspective. *Journal of Petrology* **56**, 409-439.

Tatsumi, Y. & Suzuki, T. (2009) Tholeiitic vs calc-alkalic differentiation and evolution of arc crust: Constraints from melting experiments on a basalt from the Izu–Bonin–Mariana arc. *Journal of Petrology* **50**, 1575-1603.

Taylor, B. (1992) Rifting and the volcanic-tectonic evolution of the Izu–Bonin–Mariana Arc. *Proceedings of the Ocean Drilling Program, Scientific Results* **126**, 627-651.

Taylor, B. & Goodliffe, A. M. (2004) The West Philippine Basin and the initiation of subduction, revised. *Geophysical Research Letters* **31**:L12602.

Temple, M., Filzmoser, P. & Reimann, C. (2008) Cluster analysis applied to regional geochemical data: Problems and possibilities. *Applied Geochemistry* **23**, 2198-2213.

Tormey, D. R., Grove, T. L. & Bryan, W. B. (1987) Experimental petrology of normal MORB near Kane Fracture Zone: 22º–25 ºN, mid-Atlantic ridge. *Contributions to Mineralogy and Petrology* **96**, 121-139.

Ueda, H., Sawaki, Y. & Maruyama, S. (2017) Reactions between olivine and CO_2-rich seawater at 300 °C: Implications for H_2 generation and CO_2 sequestration on the early Earth. *Geoscience Frontiers* **8**, 387-396.

Ueki, K., Hino, H. & Kuwatani, T. (2018) Geochemical discrimination and characteristics of magmatic tectonic settings: a machine-learning-based approach. *Geochemistry, Geophysics, Geosystems* **19**, 1327-1347. https://doi.org/10.1029/2017GC007401.

Ueki, K. & Iwamori, H. (2017) Geochemical differentiation process for arc magma of the Sengan volcanic cluster, Northeastern Japan, constrained from principal component analysis. *Lithos* **290-291**, 60-75.

Umino, S., Kitamura, K., Kanayama, K., Tamura, A., Sakamoto, N., Ishizuka, O. & Arai, S. (2015) Thermal and chemical evolution of the subarc mantle revealed by spinel-hosted melt inclusions in boninite from the Ogasawara (Bonin) Archipelago, Japan. *Geology* **43**, 151-154.

Ushioda, M., Takahashi, E., Hamada, M., Suzuki, T. & Niihori, K. (2018) Evolution of magma plumbing system in Miyakejima Volcano: Constraints from melting experiments. *Journal of Geophysical Research: Solid Earth* **123**, 8615-8636. https://doi.org/10.1029/2018JB015910

Walker, D., Shibata, T. & DeLong, S. E. (1979) Abyssal tholeiites from the Oceanographer Fracture Zone II. Phase equilibria and mixing. *Contributions to Mineralogy and Petrology* **70**, 111-125.

White, W. M. & Duncan, R. A. (1996) Geochemistry and geochronology of the Society Islands: New evidence for deep mantle recycling. In: Basu, A. & Hart, S. (eds) *Earth processes: Reading the isotopic code. Geophysical Monograph* **95**, 183-206.

Workman, R. K. & Hart, S. R. (2005) Major and trace element composition of the depleted MORB mantle (DMM). *Earth and Planetary Science Letters* **231**, 53-72.

Yasukawa, K., Nakamura, K., Fujinaga, K., Iwamori, H. & Kato, Y. (2016) Tracking the spatiotemporal variations of statistically independent components involving enrichment of rare-earth elements in deep-sea sediments. *Scientific Reports* **6**, 29603.

Yogodzinski, G. M., Bizimis, M., Hickey-Vargas, R., McCarthy, A., Hocking B. D., Savov, I. P., Ishizuka, O. & Arculus, R. (2018) Implications of Eocene-age Philippine Sea and forearc basalts for initiation and early history of the Izu–Bonin–Mariana arc. *Geochimica et Cosmochimica Acta* **228**, 136-156.

Yogodzinski, G. M., Kay, R. W., Volynets, O. N., Koloskov, A. V. & Kay, S. M. (1995) Magnesian andesite in the western Aleutian Komandorsky region: Implications for slab melting and processes in the mantle wedge. *Geological Society of America Bulletin* **107**, 505-519.

Zimmer, M. M., Plank, T., Hauri, E. H., Yogodzinski, G. M., Stelling, P., Larsen, J., Singer, B., Jicha, B., Mandeville, C. & Nye, C. J. (2010) The role of water in generating the calc-alkaline trend: New volatile data for Aleutian magmas and a new tholeiitic index. *Journal of Petrology* **51**, 2411-2444.

Zindler, A., Jagoutz, E. & Goldstein, S. (1982) Na, Sr and Pb isotopic systematics in a three-component mantle: a new perspective. *Nature* **298**, 519-523.

Figure captions

Fig. 1 Bathymetric map of the Izu–Bonin–Mariana arc-basin system in the Western Pacific, showing the location of the Amami Sankaku Basin and the Kyushu–Palau Ridge (after Arculus *et al*., 2015a & b). Blue is deeper seafloor and red is shallower one. The location of IODP Site U1438 is marked by a star.

Fig. 2 Summary of the lithostratigraphy of Hole U1438 and sampling depths. mbsf = meters below seafloor; cl = clay (<2^{-8} mm, dark brown); si = silt (2^{-8}–2^{-4} mm, brown); vfs-fs = very fine sand-fine sand (2^{-4}–2^{-2} mm, light brown); ms-vcs = medium sand-very coarse sand (2^{-2}–2^{1} mm, light gray); gr = gravel (>2^{1} mm, dark gray) (after Arculus *et al.*, 2015a & Brandl *et al.*, 2017). Total of 237 melt inclusions from 48 core locations (blue filled circle) were analysed in this study. Ages of sedimentary units are based on the age-depth model of Brandl *et al*. (2017), which uses shipboard micropaleontological and paleomagnetic studies (Arculus *et al*., 2015a & b). The age range of oceanic igneous crust (46.8−49.3 Ma, whose weighted mean is 48.7 Ma) is determined by Ishizuka *et al.* (2018).

Fig. 3 Backscattered electron image of melt inclusions and their host minerals. Host

mineral IDs of (a)–(c) are listed in Supplementary Data Tables S1 and S2. (a) Plagioclase hosting melt inclusions (sample D21R1-21-1, host mineral ID: 20). (b) Clinopyroxene hosting rounded melt inclusions (sample D27R3B-min3, host mineral ID: 37) (c) Clinopyroxene hosting slightly angular melt inclusions. Shrinkage bubbles are observed in melt inclusions indicated by white arrows (sample E20R6-1, host mineral ID: 103). (d) Clinopyroxene hosting apatite inclusions (sample U1438E-50R, ~40 Ma).

Fig. 4 Variation of volatiles (H_2O, S, F and Cl) and P_2O_5 in melt inclusions plotted versus the deposition age of volcaniclastic sediments in Ma. The age is based on the age-depth model of Brandl *et al*. (2017). Analytical uncertainty of H_2O with FTIR (2σ deviation = 0.16 wt %) in (a) was determined by repeated analysis of melt inclusions. Analytical uncertainty of Cl in high-Cl melt inclusions with EPMA (2σ deviation = 200 ppm) in (d) was also determined by repeated analysis of melt inclusions. Volatiles and P_2O_5 content of other melt inclusions was analysed with SIMS. Other analytical uncertainties are 2σ deviation of repeated analysis of EPR-3G reference glass (Shimizu *et al.*, 2017 & 2019) for *in situ* monitoring, which are 100 ppm for H_2O, 2 ppm for F, 4 ppm for Cl, 14 ppm for S and 30 ppm for P_2O_5. They are smaller than symbol size.

Fig. 5 Variation of volatile element content (H_2O, S, F and Cl) of melt inclusions plotted versus selected major element oxides (SiO_2, FeO_t and K_2O). FeO_t in (c) is total iron oxides ($FeO + Fe_2O_3$). Major element compositions (SiO_2, FeO_t and K_2O) are normalised to 100 wt % total without volatiles. Analytical uncertainties of major element oxides are 2σ deviation of repeated analyses of MPI-DING reference glasses (Jochum *et al*., 2000) with EPMA for *in situ* monitoring. Analytical uncertainties of volatiles are smaller than symbol size.

Fig. 6 (a) Contribution of each eigenvalue. The number of eigenvectors that individually account for ≥ 5% of the variance for the dataset of 237 melt inclusions is 5. (b) Cumulative contribution of eigenvalues. The cumulative contribution of the first five eigenvectors accounts for ~90 % of the variance.

Fig. 7 Results of K-means cluster analysis (KCA) plotted on oxide variation diagrams in wt %. Major element compositions are normalised to 100 wt % total without volatiles. Analytical uncertainties are 2σ deviation of repeated analysis of MPI-DING reference glasses (Jochum *et al*., 2000) with EPMA. The tholeiitic/calc-alkaline dividing line in (d) is from Miyashiro (1974), where FeO_t is total iron oxides ($FeO + Fe_2O_3$). The definition

of low-K, medium-K and high-K series in (g) is after Gill (1981).

Fig. 8 Results of KCA. (a) Summary of downhole distribution of melt inclusions within the drill cores. Data points connected by a tie line denote a pair of melt inclusion clusters sampled from the same core samples. The age is based on the age-depth model of Brandl *et al*. (2017). (b) Summary of coexistence of clusters within a single host mineral. Data points connected by a tie line denote melt inclusion pairs hosted in a single host mineral. ID number is "host mineral ID" listed in Table 1 and Supplementary Data Tables S1 and S2.

Fig. 9 (a−e) Representative back-scattered electron images of host clinopyroxene minerals and melt inclusions, where melt inclusions are assigned to different clusters in a host mineral. Host mineral ID is listed in Table 1 and Supplementary Data Tables S1 and S2. See main text for a detained description.

Fig. 10 Result of KCA plotted on major element or volatile element composition versus age (in Ma). The age is based on the age-depth model of Brandl *et al*. (2017). Major element compositions are normalised to 100 wt % total without volatiles. Analytical

uncertainties of major element oxides are 2σ deviation of repeated analysis with EPMA.

Fig. 11 Schematic diagram showing an overview of the occurrence of each cluster with age (in Ma).

Fig. 12 (a, b, d and e) Variations in volatiles (H_2O, S, F and Cl, respectively) versus selected major element oxides (SiO_2, FeO_t and K_2O). (c) Variation in H_2O versus S. (f) Variation in F/P (wt ratio) versus SiO_2. Major element compositions are normalised to 100 wt % total without volatiles. Analytical uncertainties of major element oxides are 2σ deviation of repeated analysis with EPMA.

Fig. 13 (a−c) Depleted MORB Mantle (DMM)-normalised trace earth element patterns for melt inclusions assigned to Clusters 1, 2b, 3b and 4a. Data of trace element compositions are from Brandl *et al*. (2017). (d−f) DMM-normalised trace earth element patterns for volcanic rocks from the proto-IBM arc. Data of trace element compositions are from Kanayama *et al*. (2014) and Umino *et al*. (2015). Normalising values for DMM are from Workman & Hart (2005).

Fig. 14 (a, b) Comparison of F and Cl content of melt inclusions reported from the fore-arc sites of the IBM arc by Straub *et al*. (2003a & b) and (c, d) melt inclusions from IODP Site U1438 (this study). Analytical uncertainties of MgO in (c) and (d) are 2σ deviation of repeated analysis with EPMA.

Fig. 15 (a) A molar ratio plot for melt inclusions. (b) H_2O versus SiO_2 for Cluster 3b melt inclusions. (c) Al_2O_3 versus SiO_2 for Cluster 3b melt inclusions. Analytical uncertainties of SiO_2 in (b) and (c) are 2σ deviation of repeated analysis with EPMA.

Fig. 16 Projections of normative composition of melt inclusions from the plagioclase apex for (a) Cluster 1 melt inclusions, (b) Cluster 2b melt inclusions, and (c) Cluster 3b melt inclusions.

Fig. 17 Results of thermodynamic modelling using COMAGMAT 3.72 starting from the most undifferentiated Cluster 1 melt inclusion (U1438E-27R5W56-I11), plotted with geochemical variation of Cluster 1 melt inclusions. Analytical uncertainties are 2σ deviation of repeated analysis with EPMA.

Fig. 18 Results of thermodynamic modelling using COMAGMAT 3.72 starting from the most undifferentiated Cluster 2b melt inclusion (U1438D-60R4-I1), plotted with geochemical variation of Cluster 2b melt inclusions. Analytical uncertainties are 2σ deviation of repeated analysis with EPMA.

Fig. 19 Results of thermodynamic modelling using COMAGMAT 3.72 starting from the most undifferentiated Cluster 3b melt inclusion (low-H_2O subgroup; U1438D-63R1W-I6), plotted with geochemical variation of Cluster 3b melt inclusions (low-H_2O subgroup). Analytical uncertainties are 2σ deviation of repeated analysis with EPMA.

Fig. 20 Results of thermodynamic modelling using COMAGMAT 3.72 starting from the most undifferentiated Cluster 3b melt inclusion (high-H_2O subgroup; D55R3A-min8-mi4), plotted with geochemical variation of Cluster 3b melt inclusions (high-H_2O subgroup). Analytical uncertainties are 2σ deviation of repeated analysis with EPMA.

Table 1 Pairs of melt inclusions hosted in a single clinopyroxene but assigned to different clusters.

Fig. S1 Comparison of results of (a) P_2O_5, (b) Cl and (c) S analyses with EPMA (horizontal axes) and SIMS (vertical axes). Error bars (2σ) represents average analytical uncertainty, which are (a) ±0.1 wt % (EPMA) versus ±0.003 wt % (SIMS) for P_2O_5, (b) ±200 ppm (EPMA) versus ±4 ppm (SIMS) for Cl, and (c) ±200 ppm (EPMA) versus ±14 ppm (SIMS) for S, respectively.

Fig. S2 Comparison of analytical results of H_2O in six silicic melt inclusions with SIMS and FTIR. Analytical results of H_2O with SIMS are systematically lower than those by FTIR with increasing SiO_2 in melt inclusions. Analytical uncertainty of H_2O with FTIR (0.16 wt %) was determined by repeated analysis of melt inclusions. Analytical uncertainty of H_2O with SIMS (2σ = 100 ppm, determined by repeated analyses of EPR-G3 reference glass; Shimizu *et al*., 2017 & 2019) are too small to indicate in this diagram.

Supplementary Data Table S1 Compositions of melt inclusions and host minerals. Analytical results of H_2O, S, F, Cl and P_2O_5 with SIMS and H_2O with FTIR are additional results to the initial dataset of Brandl *et al*. (2017, http://dx.doi.org/10.1016/j.epsl.2016.12.027). Brandl *et al.* (2017) is an open access article under the CC BY license (http://creativecommons.org/licenses/by/4.0/). We used

Cl content in bold on yellow background for discussion when Cl content analysed with both EPMA and SIMS are available. We used H_2O content in bold on orange background for discussion when H_2O content analysed with both SIMS and FTIR are available. See main text for a detailed description.

Supplementary Data Table S2 Results of statistical analysis of the 237 melt inclusions by K-means cluster analysis, including their principal components and independent components.

Supplementary Appendix

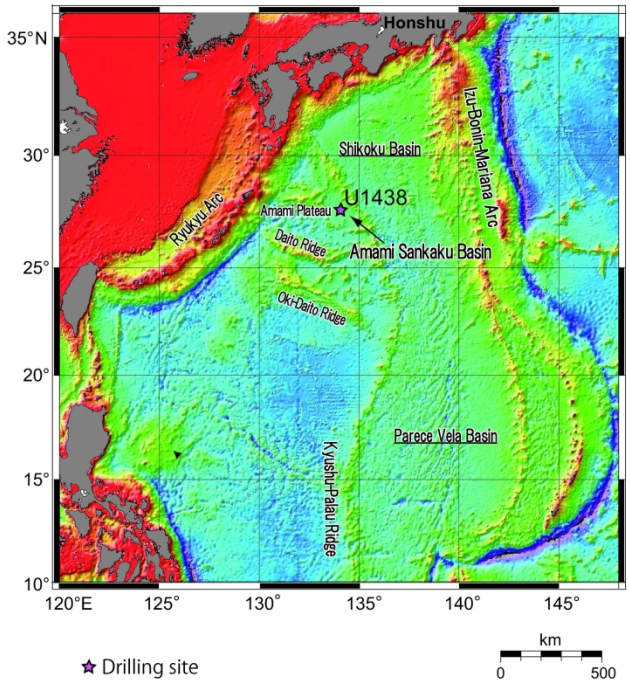

Fig. 1

Bathymetric map of the Izu–Bonin–Mariana arc-basin system in the Western Pacific, showing the location of the Amami Sankaku Basin and the Kyushu–Palau Ridge (after Arculus *et al.*, 2015a & b). Blue is deeper seafloor and red is shallower one. The location of IODP Site U1438 is marked by a star.

227x291mm (300 x 300 DPI)

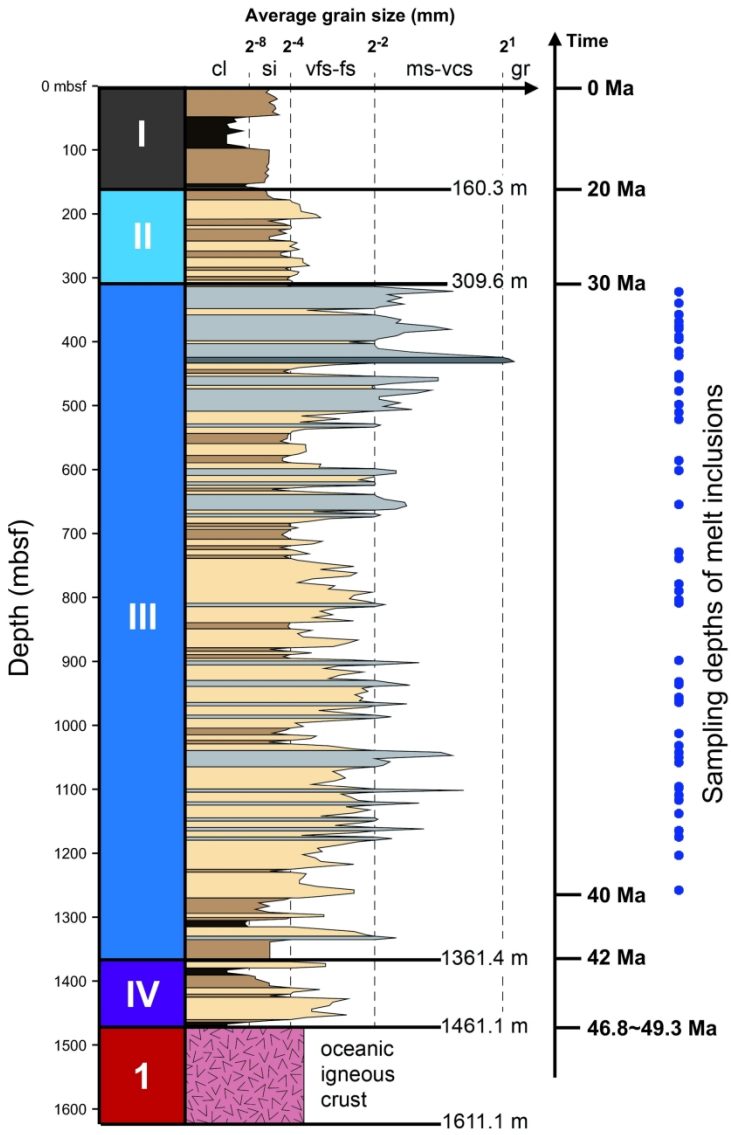

Fig. 2

Summary of the lithostratigraphy of Hole U1438 and sampling depths. mbsf = meters below seafloor; cl = clay (<2^{-8} mm, dark brown); si = silt (2^{-8}–2^{-4} mm, brown); vfs-fs = very fine sand-fine sand (2^{-4}–2^{-2} mm, light brown); ms-vcs = medium sand-very coarse sand (2^{-2}–2^{1} mm, light gray); gr = gravel (>2^{1} mm, dark gray) (after Arculus *et al*., 2015a & Brandl *et al*., 2017). Total of 237 melt inclusions from 48 core locations (blue filled circle) were analysed in this study. Ages of sedimentary units are based on the age-depth model of Brandl *et al*. (2017), which uses shipboard micropaleontological and paleomagnetic studies (Arculus *et al*., 2015a & b). The age range of oceanic igneous crust (46.8–49.3 Ma, whose weighted mean is 48.7 Ma) is determined by Ishizuka *et al*. (2018).

189x279mm (300 x 300 DPI)

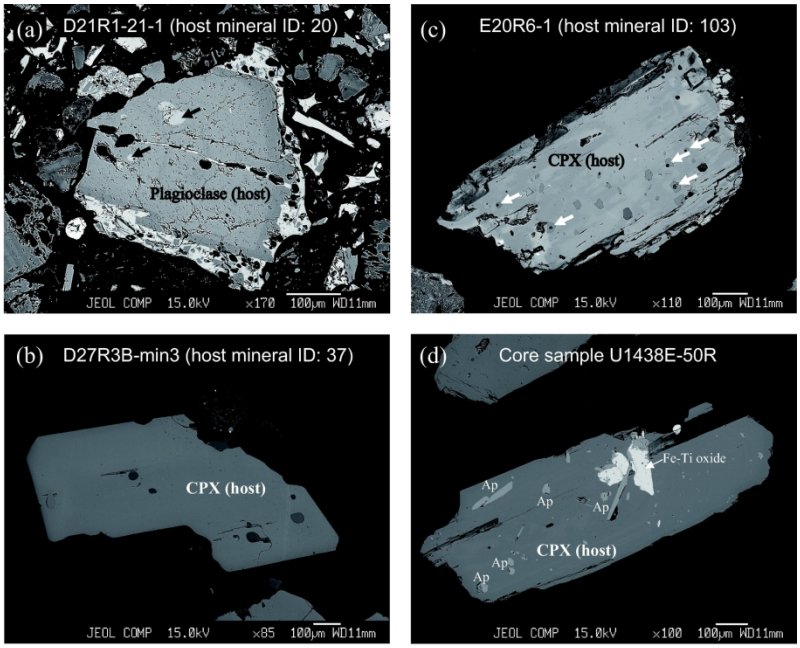

Fig. 3

Backscattered electron image of melt inclusions and their host minerals. Host mineral IDs of (a)–(c) are listed in the Supplementary Data Tables S1 and S2. (a) Plagioclase hosting melt inclusions (sample D21R1-21-1, host mineral ID: 20). (b) Clinopyroxene hosting rounded melt inclusions (sample D27R3B-min3, host mineral ID: 37) (c) Clinopyroxene hosting slightly angular melt inclusions. Shrinkage bubbles are observed in melt inclusions indicated by white arrows (sample E20R6-1, host mineral ID: 103). (d) Clinopyroxene hosting apatite inclusions (sample U1438E-50R, ~40 Ma).

175x250mm (300 x 300 DPI)

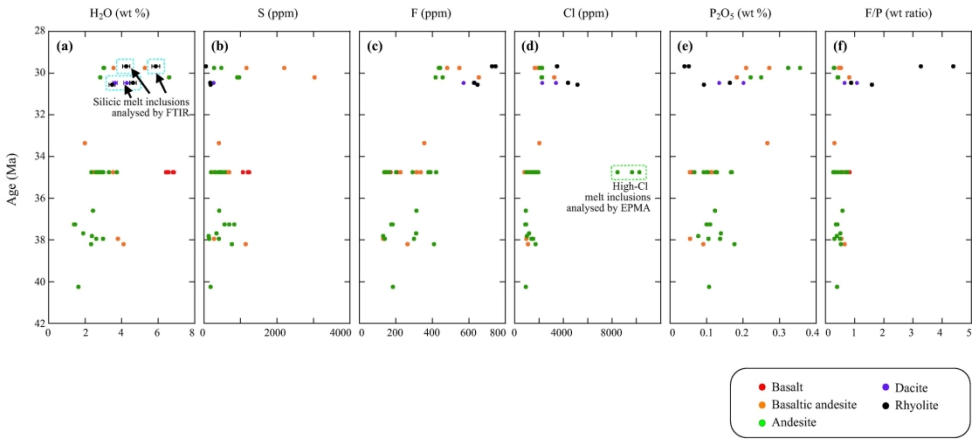

Fig. 4

Variation of volatiles (H_2O, S, F and Cl) and P_2O_5 in melt inclusions plotted versus the deposition age of volcaniclastic sediments in Ma. The age is based on the age-depth model of Brandl *et al*. (2017). Analytical uncertainty of H_2O with FTIR (2σ deviation = 0.16 wt %) in (a) was determined by repeated analysis of melt inclusions. Analytical uncertainty of Cl in high-Cl melt inclusions with EPMA (2σ deviation = 200 ppm) in (d) was also determined by repeated analysis of melt inclusions. Volatiles and P_2O_5 content of other melt inclusions was analysed with SIMS. Other analytical uncertainties are 2σ deviation of repeated analysis of EPR-3G reference glass (Shimizu *et al*., 2017 & 2019) for *in situ* monitoring, which are 100 ppm for H_2O, 2 ppm for F, 4 ppm for Cl, 14 ppm for S and 30 ppm for P_2O_5. They are smaller than symbol size.

195x200mm (300 x 300 DPI)

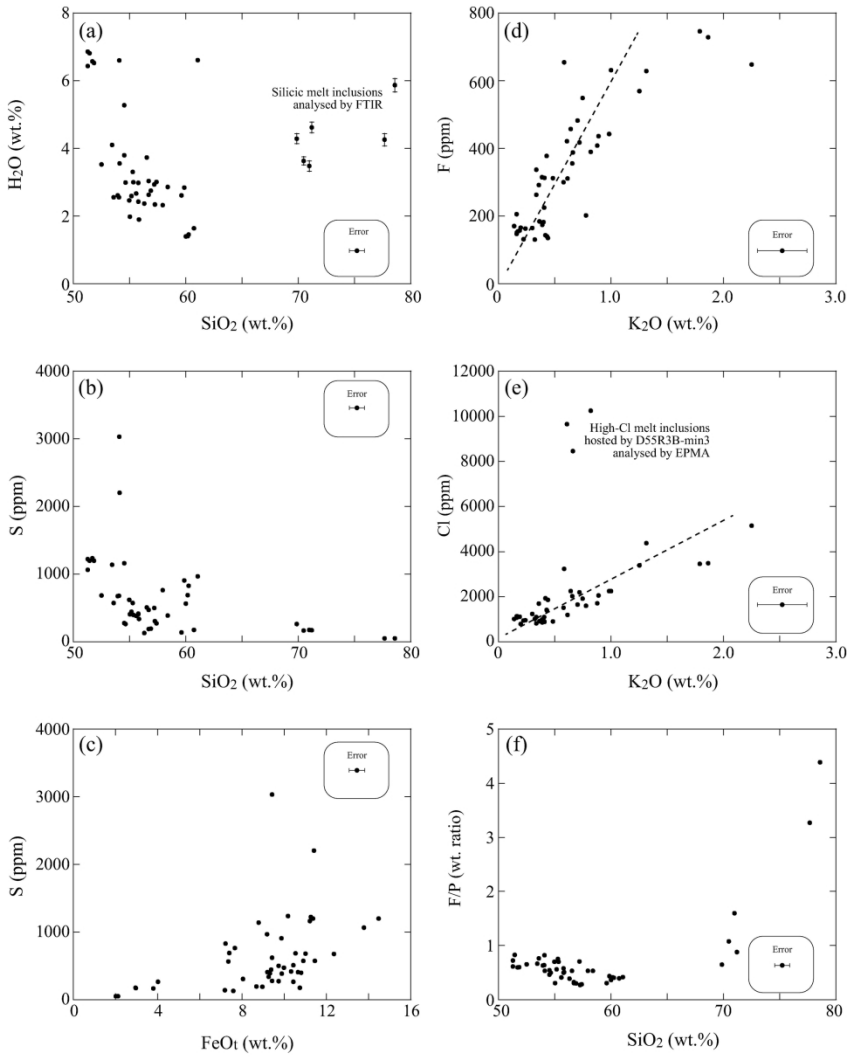

Fig. 5

Variation of volatile element content (H_2O, S, F and Cl) of melt inclusions plotted versus selected major element oxides (SiO_2, FeO_t and K_2O). FeO_t in (c) is total iron oxides (FeO + Fe_2O_3). Major element compositions (SiO2, FeO_t and K_2O) are normalised to 100 wt % total without volatiles. Analytical uncertainties of major element oxides are 2σ deviation of repeated analyses of MPI-DING reference glasses (Jochum *et al*., 2000) with EPMA for *in situ* monitoring. Analytical uncertainties of volatiles are smaller than symbol size.

197x270mm (300 x 300 DPI)

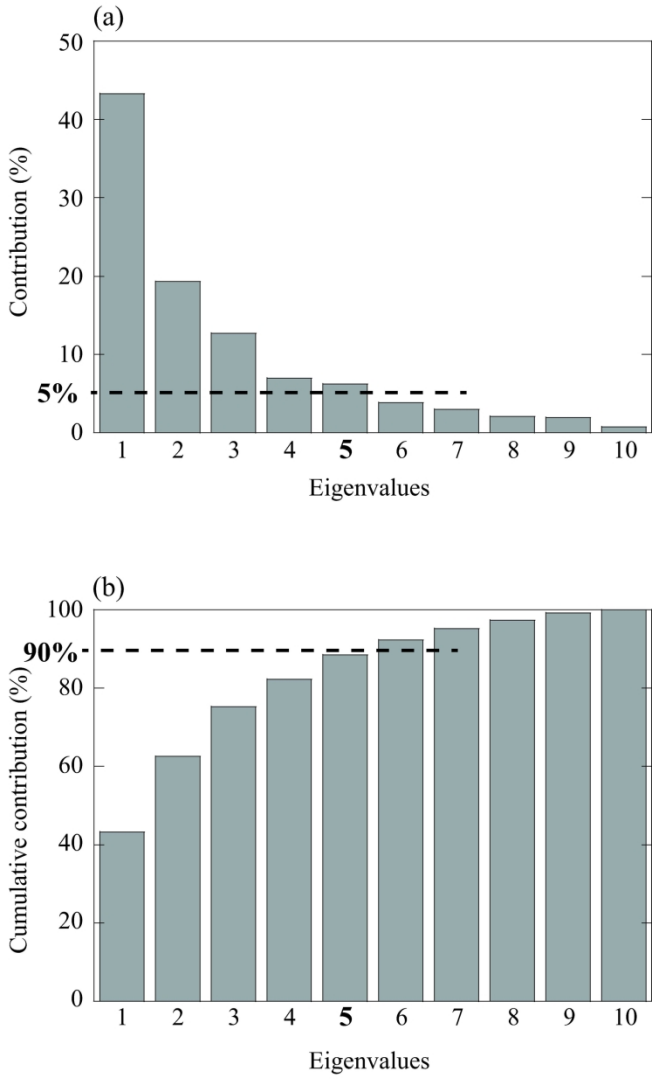

Fig. 6

(a) Contribution of each eigenvalue. The number of eigenvectors that individually account for ≥ 5% of the variance for the dataset of 237 melt inclusions is 5. (b) Cumulative contribution of eigenvalues. The cumulative contribution of the first five eigenvectors accounts for ~90 % of the variance.

173x272mm (300 x 300 DPI)

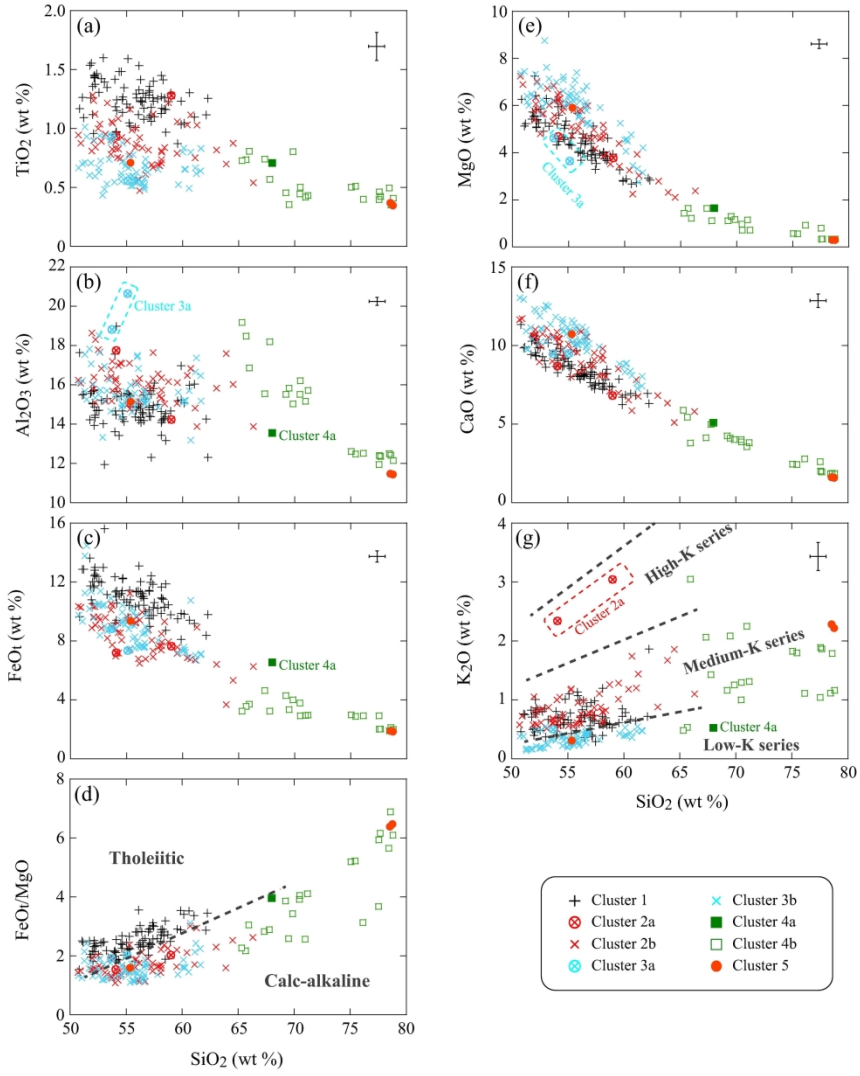

Fig. 7

Results of K-means cluster analysis (KCA) plotted on oxide variation diagrams in wt %. Major element compositions are normalised to 100 wt % total without volatiles. Analytical uncertainties are 2σ deviation of repeated analysis of MPI-DING reference glasses (Jochum *et al.*, 2000) with EPMA. The tholeiitic/calc-alkaline dividing line in (d) is from Miyashiro (1974), where total FeO_t is total iron oxides (FeO + Fe_2O_3). The definition of low-K, medium-K and high-K series in (g) is after Gill (1981).

196x271mm (300 x 300 DPI)

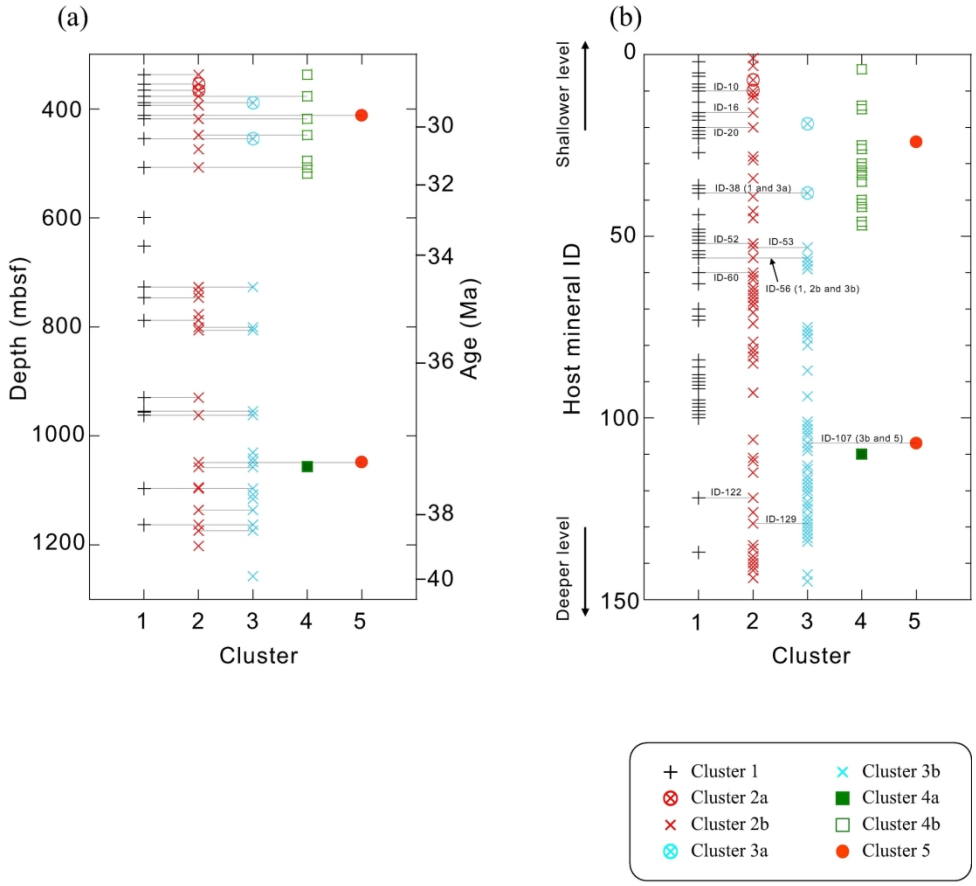

Fig. 8

Results of KCA. (a) Summary of downhole distribution of melt inclusions within the drill cores. Data points connected by a tie line denote a pair of melt inclusion clusters sampled from the same core samples. The age is based on the age-depth model of Brandl *et al*. (2017). (b) Summary of coexistence of clusters within a single host mineral. Data points connected by a tie line denote melt inclusion pairs hosted in a single host mineral. ID number is "host mineral ID" listed in Table 1 and Supplementary Data Tables S1 and S2.

186x223mm (300 x 300 DPI)

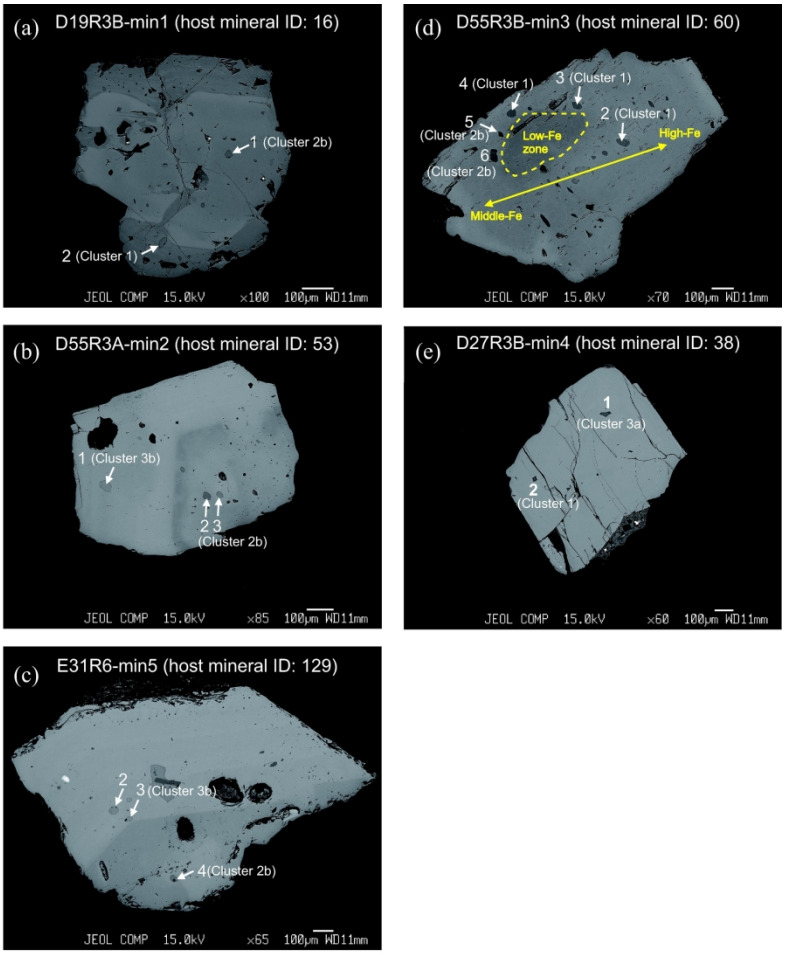

Fig. 9

(a–e) Representative back-scattered electron images of host clinopyroxene minerals and melt inclusions, where melt inclusions are assigned to different clusters in a host mineral. Host mineral ID is listed in Table 1 and Supplementary Data Tables S1 and S2. See main text for a detained description.

175x255mm (300 x 300 DPI)

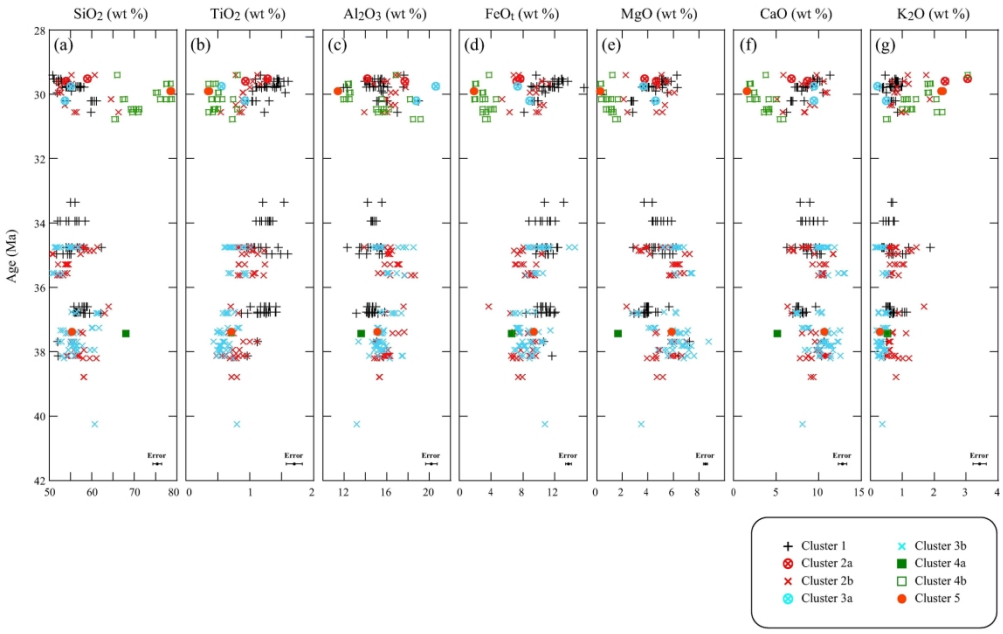

Fig. 10

Result of KCA plotted on major element or volatile element composition versus age (in Ma). The age is based on the age-depth model of Brandl *et al*. (2017). Major element compositions are normalised to 100 wt % total without volatiles. Analytical uncertainties of major element oxides are 2σ deviation of repeated analysis with EPMA.

197x206mm (300 x 300 DPI)

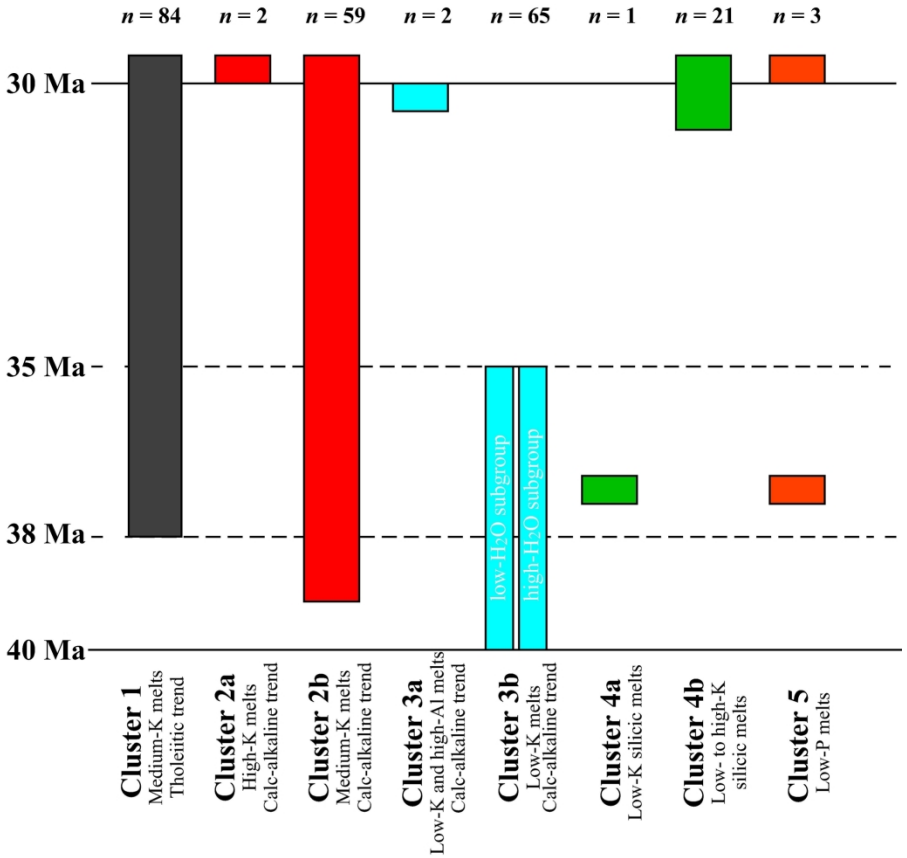

Fig. 11

Schematic diagram showing an overview of the occurrence of each cluster with age (in Ma).

186x232mm (300 x 300 DPI)

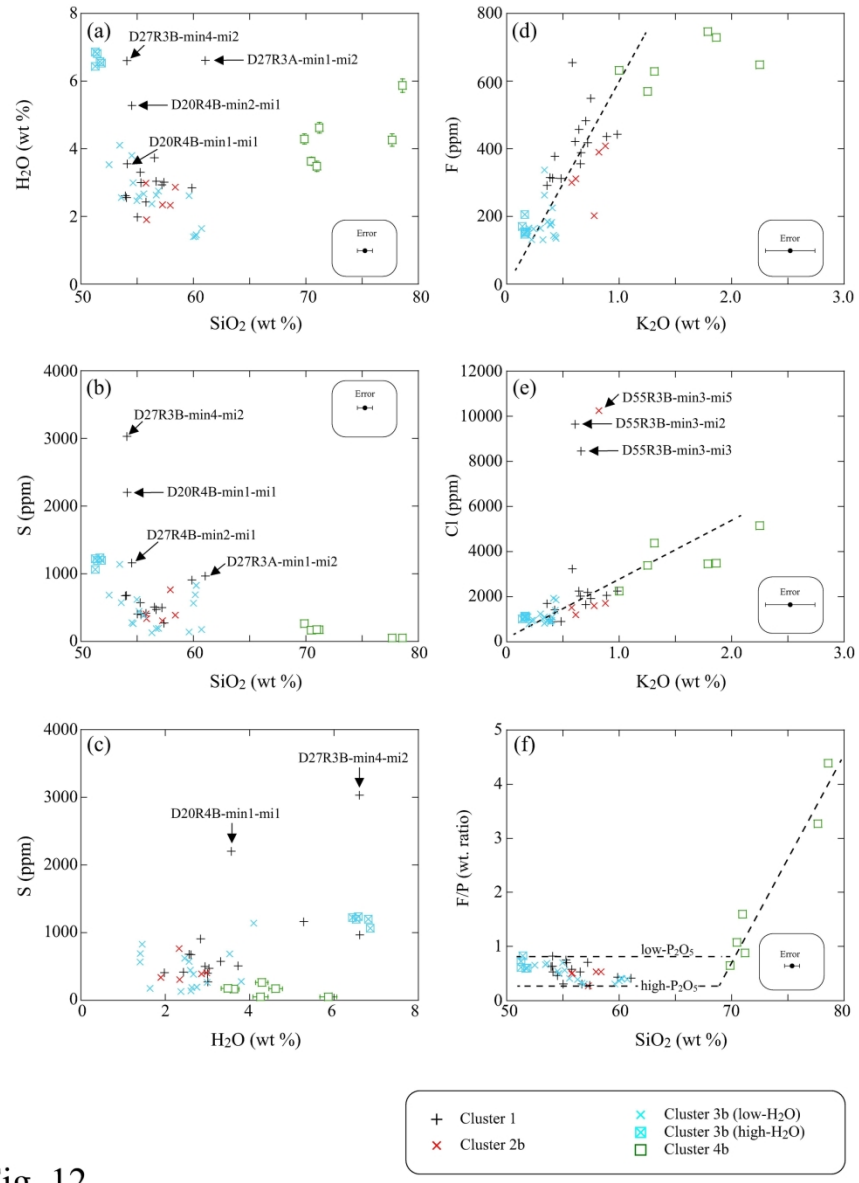

Fig. 12

(a, b, d and e) Variations in volatiles (H_2O, S, F and Cl, respectively) versus selected major element oxides (SiO_2, FeO_t and K_2O). (c) Variation in H_2O versus S. (f) Variation in F/P (wt ratio) versus SiO_2. Major element compositions are normalised to 100 wt % total without volatiles. Analytical uncertainties of major element oxides are 2σ deviation of repeated analysis with EPMA.

197x270mm (300 x 300 DPI)

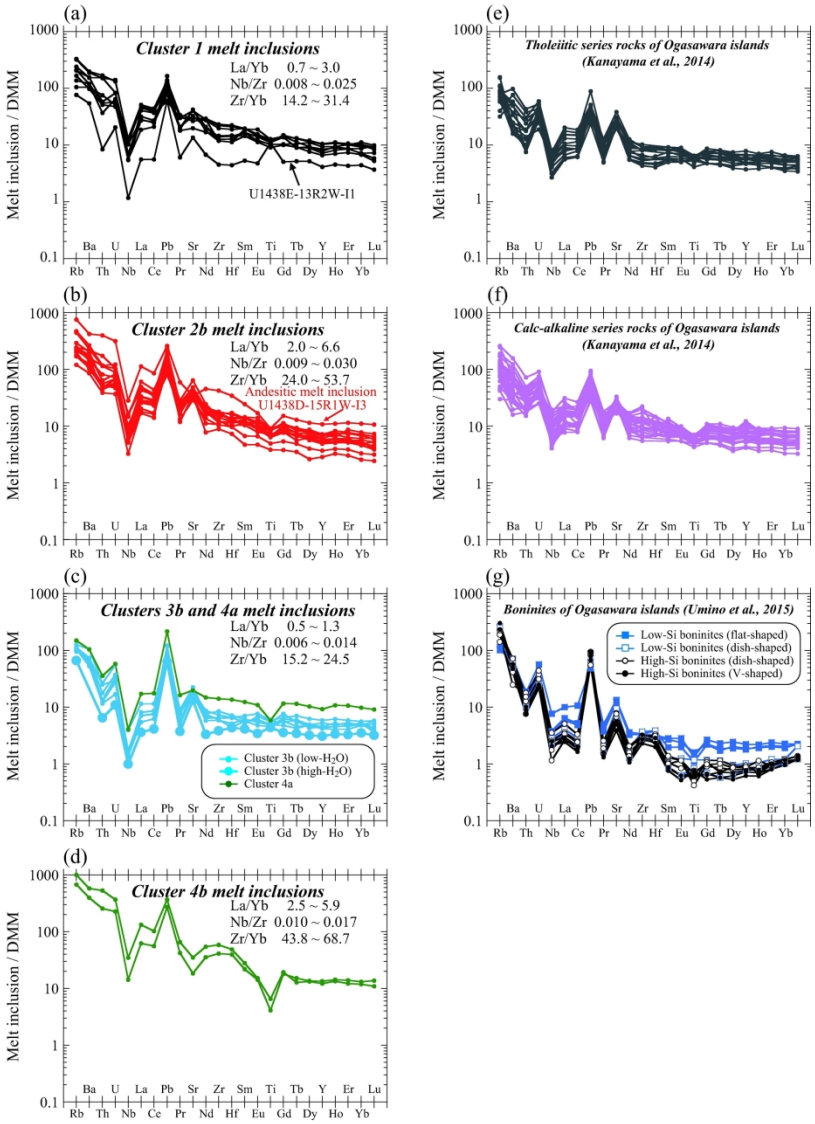

Fig. 13

(a–c) Depleted MORB Mantle (DMM)-normalised trace earth element patterns for melt inclusions assigned to Clusters 1, 2b, 3b and 4a. Data of trace element compositions are from Brandl *et al*. (2017). (d–f) DMM-normalised trace earth element patterns for volcanic rocks from the proto-IBM arc. Data of trace element compositions are from Kanayama *et al*. (2014) and Umino *et al*. (2015). Normalising values for DMM are from Workman & Hart (2005).

194x282mm (300 x 300 DPI)

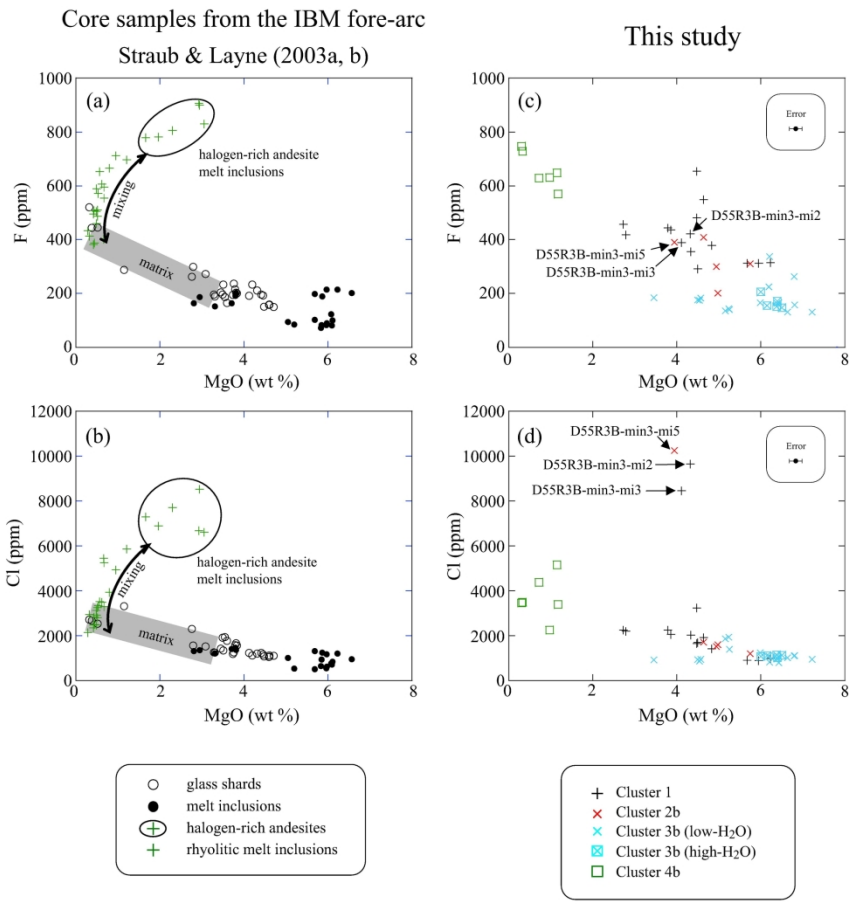

Fig. 14

(a, b) Comparison of F and Cl content of melt inclusions reported from the fore-arc sites of the IBM arc by Straub *et al*. (2003a & b) and (c, d) melt inclusions from IODP Site U1438 (this study). Analytical uncertainties of MgO in (c) and (d) are 2σ deviation of repeated analysis with EPMA.

196x271mm (300 x 300 DPI)

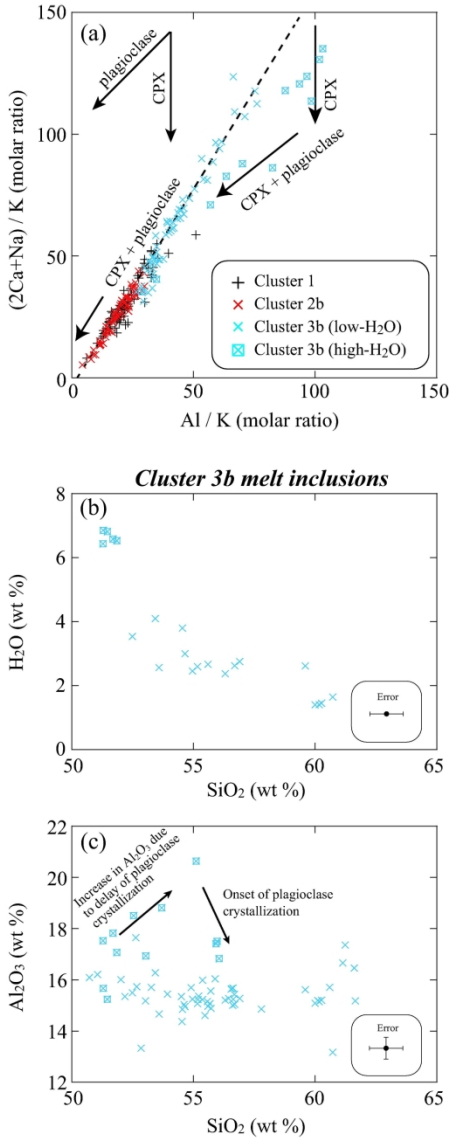

Fig. 15

(a) A molar ratio plot for melt inclusions. (b) H_2O versus SiO_2 for Cluster 3b melt inclusions. (c) Al_2O_3 versus SiO_2 for Cluster 3b melt inclusions. Analytical uncertainties of SiO_2 in (b) and (c) are 2σ deviation of repeated analysis with EPMA.

151x250mm (300 x 300 DPI)

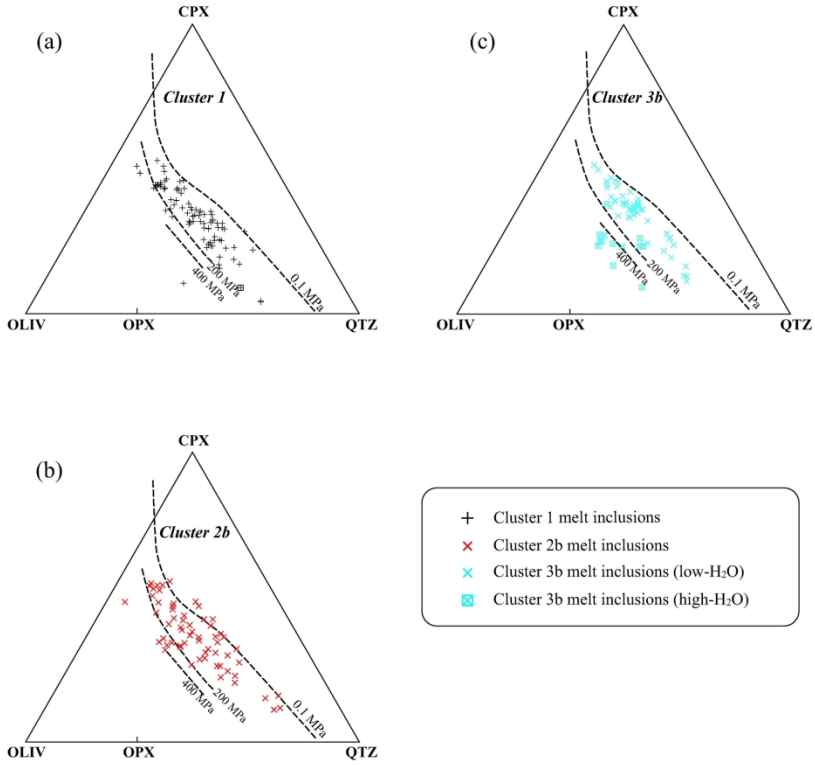

Fig. 16

Projections of normative composition of melt inclusions from the plagioclase apex for (a) Cluster 1 melt inclusions, (b) Cluster 2b melt inclusions, and (c) Cluster 3b melt inclusions.

184x251mm (300 x 300 DPI)

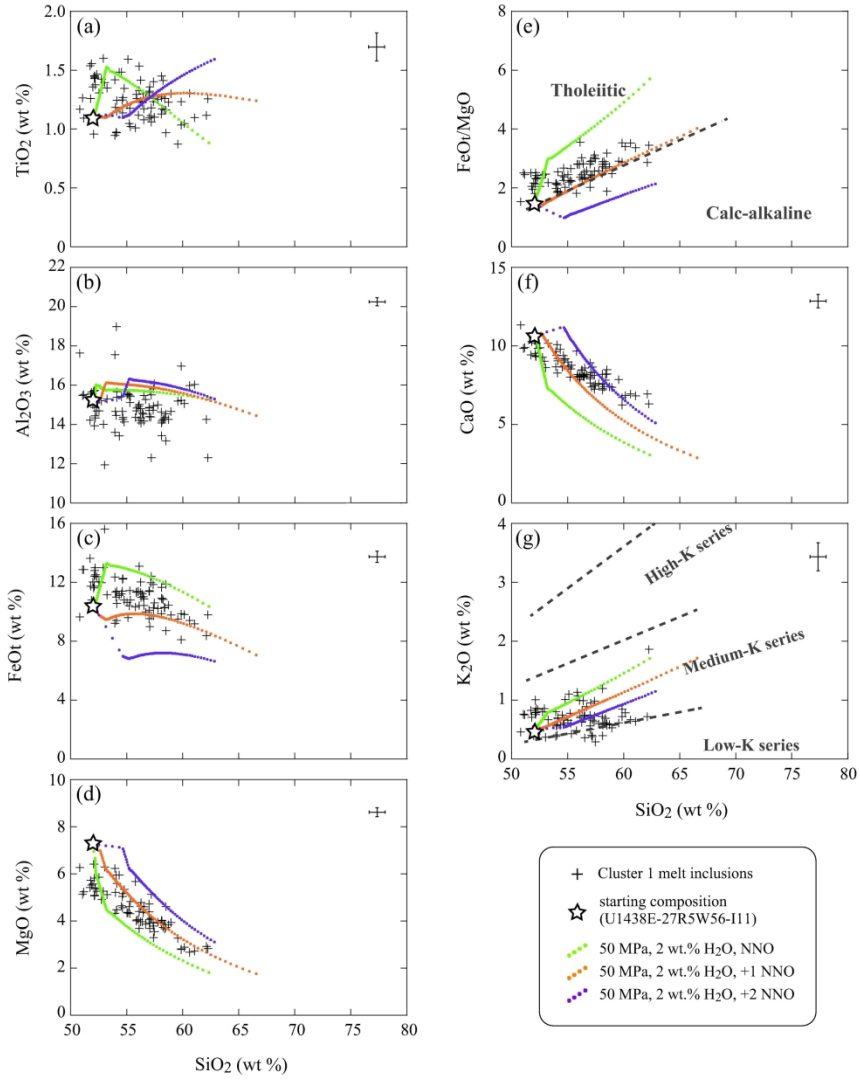

Fig. 17

Results of thermodynamic modelling using COMAGMAT 3.72 starting from the most undifferentiated Cluster 1 melt inclusion (U1438E-27R5W56-I11), plotted with geochemical variation of Cluster 1 melt inclusions. Analytical uncertainties are 2σ deviation of repeated analysis with EPMA.

196x271mm (300 x 300 DPI)

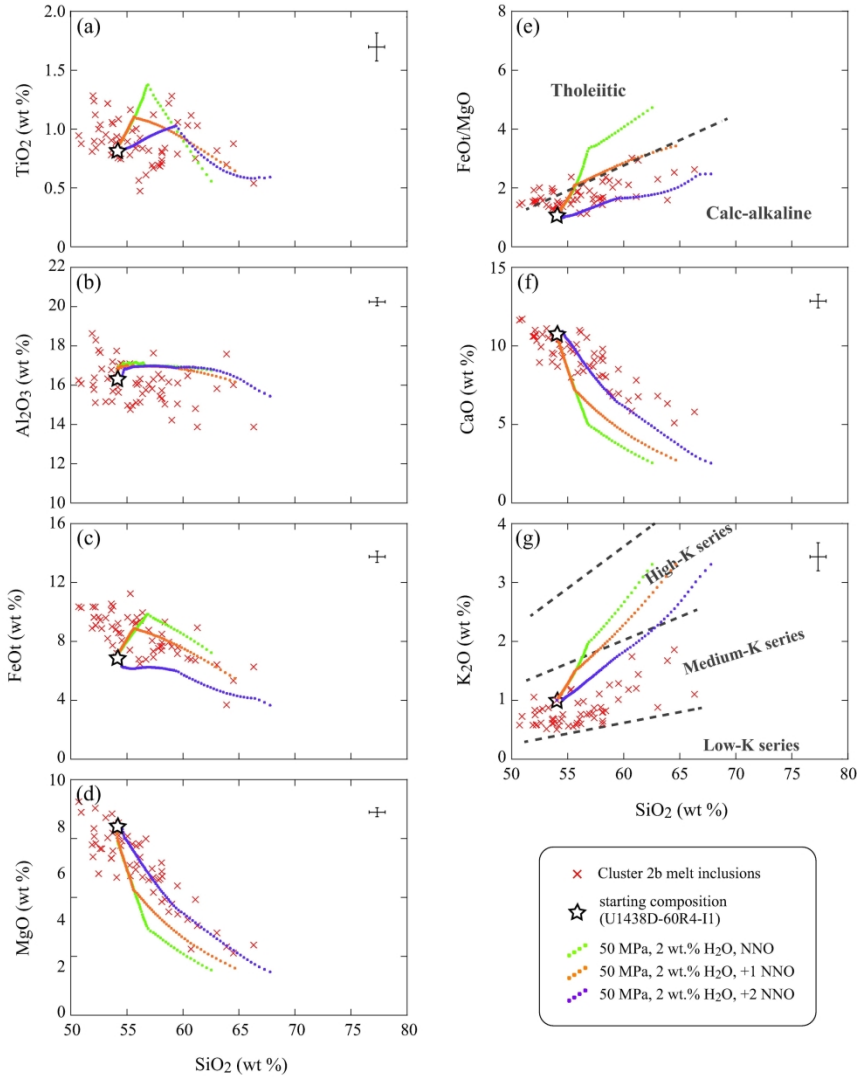

Fig. 18

Results of thermodynamic modelling using COMAGMAT 3.72 starting from the most undifferentiated Cluster 2b melt inclusion (U1438D-60R4-I1), plotted with geochemical variation of Cluster 2b melt inclusions. Analytical uncertainties are 2σ deviation of repeated analysis with EPMA.

196x271mm (300 x 300 DPI)

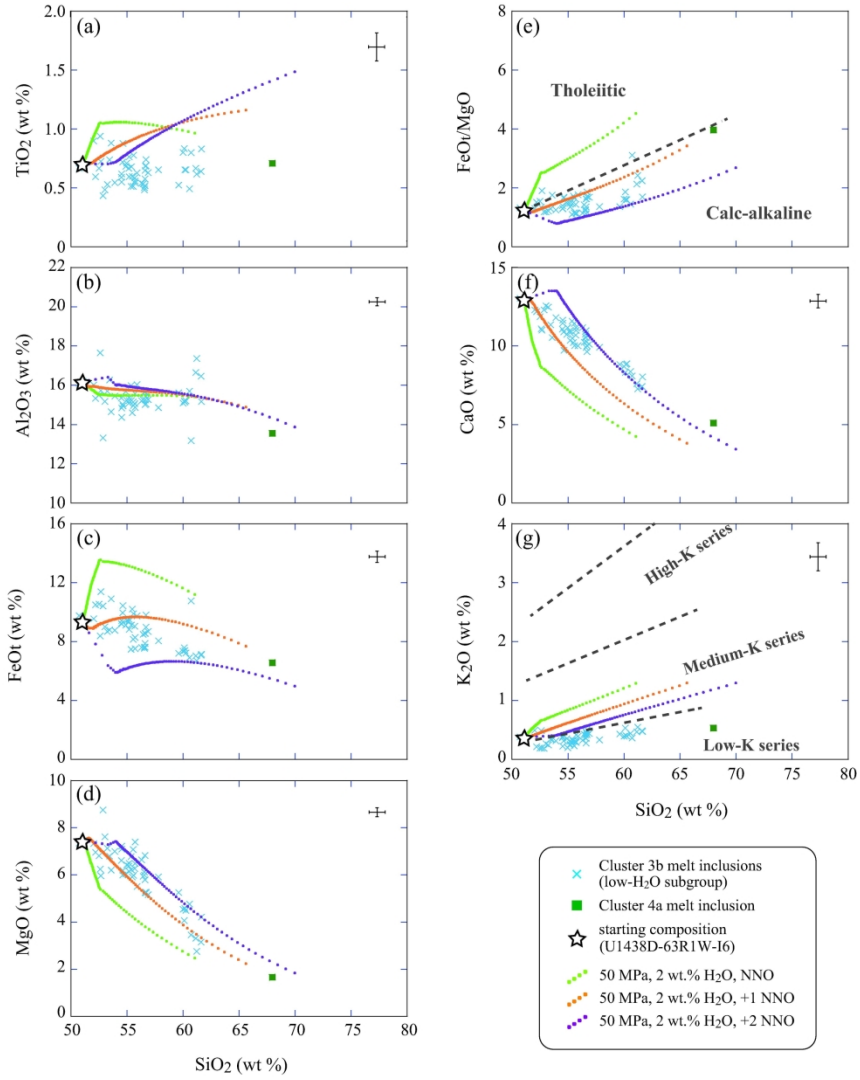

Fig. 19

Results of thermodynamic modelling using COMAGMAT 3.72 starting from the most undifferentiated Cluster 3b melt inclusion (low-H_2O subgroup; U1438D-63R1W-I6), plotted with geochemical variation of Cluster 3b melt inclusions (low-H_2O subgroup). Analytical uncertainties are 2σ deviation of repeated analysis with EPMA.

196x271mm (300 x 300 DPI)

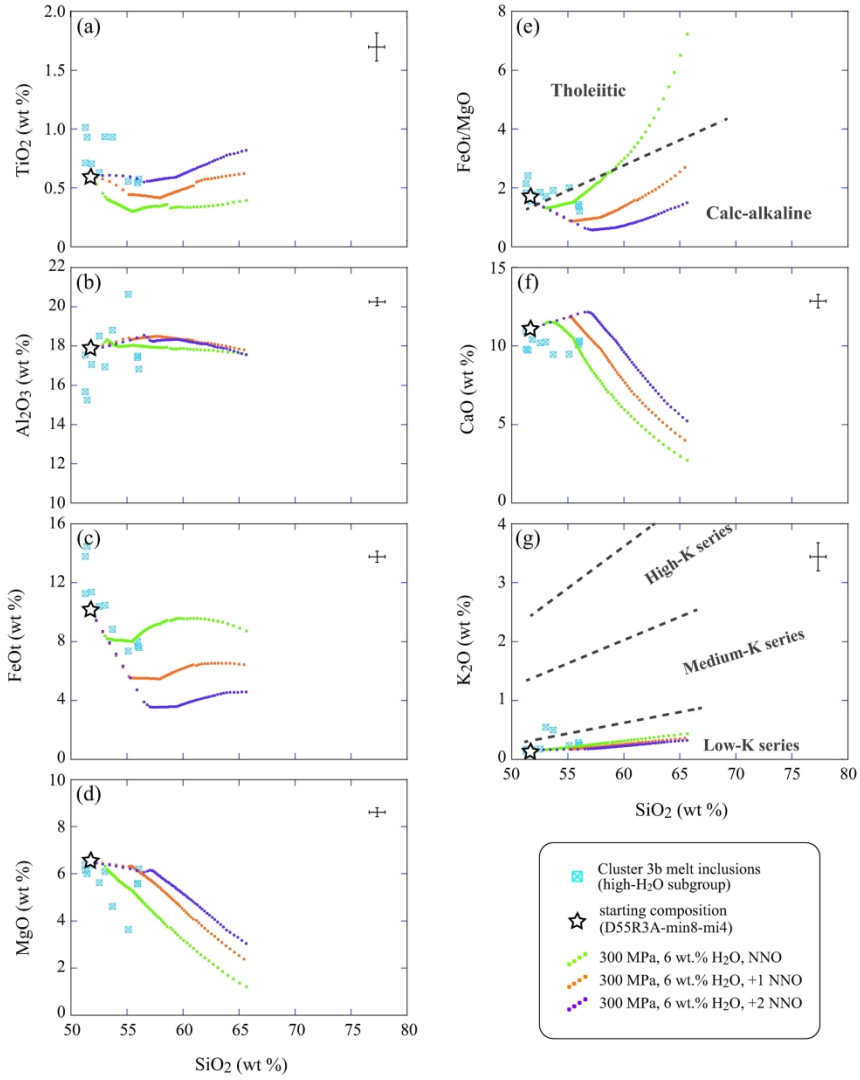

Fig. 20

Results of thermodynamic modelling using COMAGMAT 3.72 starting from the most undifferentiated Cluster 3b melt inclusion (high-H_2O subgroup; D55R3A-min8-mi4), plotted with geochemical variation of Cluster 3b melt inclusions (high-H_2O subgroup). Analytical uncertainties are 2σ deviation of repeated analysis with EPMA.

196x271mm (300 x 300 DPI)

Host mineral ID	10		16		20		38	
Melt inclusion ID	U1438D-18R2W-I7	U1438D-18R2W-I8	D-19R3B-min1-mi1	D-19R3B-min1-mi2	D21R1-21-1-I1	D21R1-21-1-I2	D27R3B-min4-mi1	D27R3B-min4-mi2
Cluster	2a	1	2b	1	1	2b	3a	1
SiO_2	53.2	53.1	54.2	53.0	51.7	49.8	48.5	49.1
TiO_2	0.92	1.22	1.14	1.23	1.36	0.95	0.84	0.88
Al_2O_3	17.4	15.1	14.5	13.9	16.8	16.9	17.0	17.2
FeO_t	7.08	10.4	11.0	11.9	8.86	9.17	8.0	8.6
MnO	0.14	0.16	0.23	0.24	0.18	0.19	0.16	0.22
MgO	4.60	5.49	4.63	5.01	4.15	4.56	4.17	4.06
CaO	8.55	8.89	7.82	8.47	8.32	8.50	8.55	7.51
Na_2O	3.53	2.98	2.97	2.43	3.44	3.89	2.52	2.52
K_2O	2.30	0.67	1.16	0.59	0.77	0.78	0.45	0.53
P_2O_5	0.56	0.17	0.33	0.14	0.25	0.20	0.15	0.16
Total	98.24	98.15	97.90	97.01	95.90	94.92	90.26	90.76

Host mineral ID	52			53		
Melt inclusion ID	D55R3-4-I1	D55R3-4-I2	D55R3-4-I3	D55R3A-min2-mi1	D55R3A-min2-mi2	D55R3A-min2-mi3
Cluster	2b	1	1	3b	2b	2b
SiO_2	60.7	61.4	57.4	52.3	55.2	54.2
TiO_2	1.02	1.24	1.43	0.84	0.67	0.89
Al_2O_3	13.8	12.1	13.3	14.3	15.3	14.6
FeO_t	8.9	9.7	10.8	9.98	7.76	9.1
MnO	0.24	0.23	0.22	0.26	0.14	0.15
MgO	3.01	2.80	3.84	5.93	4.80	5.18
CaO	6.72	6.22	7.18	9.31	8.39	8.54
Na_2O	3.27	2.93	3.12	2.29	3.29	3.15
K_2O	1.43	1.84	1.18	0.39	0.75	0.58
P_2O_5	0.09	0.18	0.32	0.09	0.16	0.10
Total	99.13	98.64	98.69	95.70	96.46	96.48

Host mineral ID	56				60				
Melt inclusion ID	D55R3A-min7-mi1	D55R3A-min7-mi2	D55R3A-min7-mi3	D55R3A-min7-mi4	D55R3B-min3-mi2	D55R3B-min3-mi3	D55R3B-min3-mi4	D55R3B-min3-mi5	D55R3B-min3-mi6
Cluster	2b	1	1	3b	1	1	1	2b	2b
SiO_2	52.8	51.6	51.8	51.1	52.6	54.4	51.3	55.6	55.8
TiO_2	0.94	0.93	0.91	0.84	1.12	1.01	1.07	0.80	0.78
Al_2O_3	14.2	13.8	13.1	14.0	14.4	14.7	13.4	14.3	15.7
FeO_t	8.86	10.5	11.9	10.4	10.91	9.26	11.5	8.87	8.17
MnO	0.16	0.18	0.24	0.21	0.17	0.19	0.18	0.21	0.17
MgO	5.53	5.68	5.98	5.92	4.11	3.91	4.29	3.75	3.70
CaO	9.20	9.62	9.27	10.05	8.13	7.88	8.53	7.65	7.82
Na_2O	2.77	2.66	2.46	2.45	3.06	2.99	2.91	3.10	3.18
K_2O	0.53	0.39	0.37	0.32	0.58	0.63	0.63	0.78	0.62
P_2O_5	0.12	0.08	0.07	0.09	0.12	0.10	0.11	0.14	0.11
Total	95.14	95.43	96.04	95.32	95.22	95.08	93.93	95.19	96.10

Host mineral ID	107			122		129		
Melt inclusion ID	U1438E-22R6W-I3	U1438E-22R6W-I4	U1438E-22R6W-I5	U1438E-27R5W56-I10	U1438E-27R5W56-I11	E31R6-5-mi2	E31R6-5-mi3	E31R6-5-mi4
Cluster	3b	3b	5	2b	1	3b	3b	2b
SiO_2	54.6	56.1	54.6	50.7	50.6	53.5	52.6	53.7
TiO_2	0.67	0.50	0.70	1.09	1.09	0.65	0.59	0.68
Al_2O_3	15.0	15.5	14.9	14.7	14.7	14.6	15.1	14.5
FeO_t	9.01	7.57	9.2	10.04	10.27	9.25	9.18	7.10
MnO	0.16	0.15	0.18	0.15	0.20	0.17	0.16	0.17
MgO	6.13	5.95	5.81	6.83	7.06	4.97	5.18	4.51
CaO	10.4	10.7	10.56	10.48	10.38	9.11	9.43	9.06
Na_2O	2.32	2.36	2.30	2.55	2.36	1.58	1.45	2.01
K_2O	0.32	0.36	0.30	0.56	0.50	0.47	0.37	0.56
P_2O_5	0.02	0.04	0	0.12	0.25	0.12	0.08	0.10
Total	98.61	99.26	98.52	97.26	97.41	94.40	94.18	92.45

Table 1